iScience

Article

Mathematical modeling of ribosome competition informs testable treatment strategies for drug-tolerant cancer persister cells

Graphical abstract

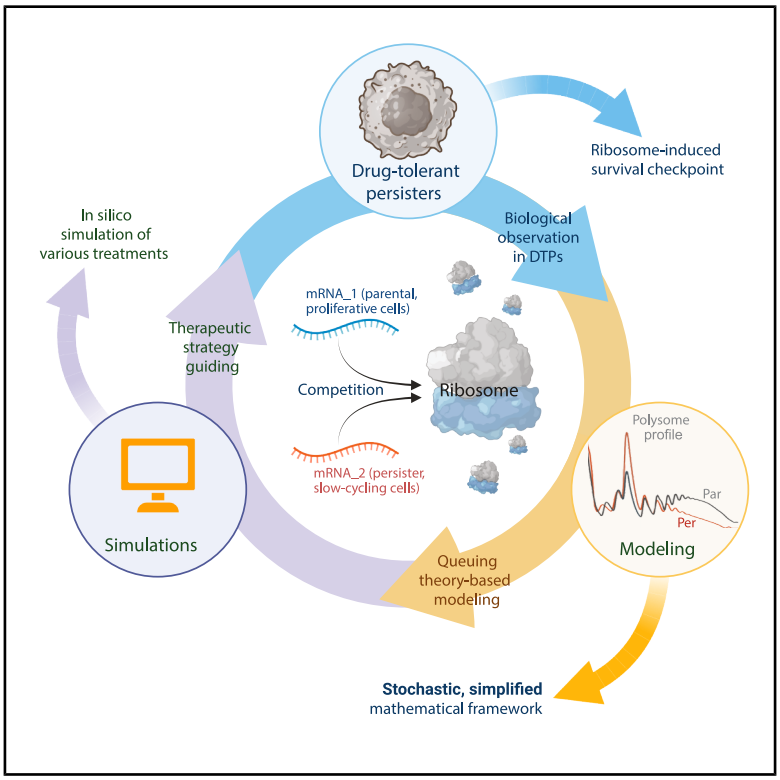

Highlights

- Translation changes in DTP cells are common across cancer types
- Reduced ribosome biogenesis creates a translational bottleneck
- Stochastic modeling reveals mRNA competition mechanisms in DTP cells
- Ribosome threshold informs strategies to delay drug resistance

Authors

Xinpu Tang (唐新璞), Yuqing Wang (王雨晴), Yi Pu, ..., Caroline Robert, Diane Peurichard, Shensi Shen (沈慎思)

Correspondence

diane.a.peurichard@inria.fr (D.P.), shensi.sean@gmail.com (S.S.)

In brief

Cancer; Mathematical biosciences; Therapy

Tang et al., 2026, iScience *29*, 115493
April 17, 2026
https://doi.org/10.1016/j.isci.2026.115493

CellPress

iScience

CellPress
OPEN ACCESS

Article

Mathematical modeling of ribosome competition informs testable treatment strategies for drug-tolerant cancer persister cells

Xinpu Tang (唐新璞),[1,10] Yuqing Wang (王雨晴),[1,10] Yi Pu,[1,2,10] Kaixiu Li (李开秀),[1] Zheyu Ding (丁哲煜),[1] Mengyao Wang (王梦瑶),[1] Luis Almeida,[3] Michael Cerezo,[4,5] Yarong Cao,[1,6] Caroline Robert,[7,8] Diane Peurichard,[9,*] and Shensi Shen (沈慎思)[1,11,*]

[1]Institute of Thoracic Oncology and National Clinical Research Center for Geriatrics, Frontiers Science Center for Disease-related Molecular Network, West China Hospital, Sichuan University, Chengdu 610000, China
[2]Department of Burn Surgery, West China Hospital, Sichuan University, Chengdu 610000, China
[3]Sorbonne Université, CNRS, Université Paris Cité, LPSM, Paris 75006, France
[4]INSERM, U1065, Equipe 12, Centre Méditerranéen de Médecine Moléculaire (C3M), Nice, France
[5]Université Côte d'Azur, Nice, France
[6]Department of Nuclear Medicine, State Key Laboratory of Biotherapy and Cancer Center, West China Hospital, Sichuan University, Chengdu 610000, China
[7]INSERM U981, Gustave Roussy Cancer Campus, Villejuif, France
[8]Université Paris-Saclay, Le Kremlin-Bicêtre, France
[9]Sorbonne Université, Inria, CNRS, Université Paris Cité, Laboratoire Jacques-Louis Lions UMR7598, Equipe MUSCLEES, Paris 75006, France
[10]These authors contributed equally
[11]Lead contact
*Correspondence: diane.a.peurichard@inria.fr (D.P.), shensi.sean@gmail.com (S.S.)
https://doi.org/10.1016/j.isci.2026.115493

SUMMARY

Systemic therapies for advanced cancers often induce initial responses but rarely achieve durable cures due to acquired resistance. Drug-tolerant persister (DTP) cells survive treatment without additional genetic mutations. We previously showed that melanoma DTP cells globally suppress mRNA translation while selectively maintaining translation of specific mRNAs, but the basis of this selectivity remained unclear. Here, we integrate stochastic modeling with experimental analyses to define the principles governing selective translation in DTP cells. We identify translational reprogramming as a conserved feature of DTP cells across cancer types and treatments. Reduced MYC-dependent ribosome biogenesis limits ribosome availability, creating a translational bottleneck. Modeling reveals that ribosome scarcity drives competition among mRNAs, thereby shaping selective translation. This framework uncovers a ribosome-dependent survival checkpoint in DTP cells and highlights ribosome thresholds as a potential vulnerability for overcoming therapy resistance.

INTRODUCTION

Standard-of-care (SOC) therapies for advanced-stage cancers are rarely curative, with acquired resistance remaining an unresolved clinical challenge despite favorable initial responses.[1,2] Recent findings revealed that genetic changes alone cannot fully account for the development of resistance.[3] Indeed, drug-tolerant persister (DTP) cells without *de novo* genetic mutations[4] can temporarily become tolerant after initial systemic anticancer treatments, allowing them to survive until more-permanent mechanisms of resistance emerge.[5,6] We previously showed that melanoma DTP cells undergo a reversible shift in mRNA translation, correlated with N6-methyladenosine (m6A) modification in the mRNA's untranslated region (UTR). This leads to enhanced translation of certain mRNAs alongside a global reduction in protein synthesis.[7,8] However, it is unclear if this mRNA translation remodeling is a common strategy in DTP cells across various cancer types and treatment regimens, and how DTP cells selectively regulate the translation of specific mRNA subsets during SOC therapies remains unknown.

Ribosome serves as an integral but was thought to be largely passive participant in protein synthesis. However, emerging studies have linked ribosome to more selective control of mRNA translation. This is pioneered in the study of cell homeostasis and organismal development.[9] In mouse tissue patterning, selective translation of *Hox* mRNAs is controlled by RPL38/eL38-containing ribosomal large subunit.[10] Changes within ribosomal protein transcription levels have also been observed among different tissue and cancer types,[11] indicating that ribosome levels may vary in a context-dependent manner. In

Diamond-Blackfan anemia (DBA), global reduction in ribosome levels profoundly alters translation of a specific subset of mRNAs that impairs erythroid lineage commitment, underlying a regulatory role for ribosome levels in cellular differentiation.[12] In cancer, tumor cells rely on translational control to appropriately adapt to limited resources while maintaining cell survival and growth.[13] Allocation of these limited resources itself are sometimes used as a global regulatory mechanism that controls cooperation among various metabolic or signaling cues in model organisms.[14] A recurrent source of potential cross-talk is the competition for the processing ribosomes that control the production of proteins. Previous work in model organisms have shown that the abundance of ribosomes is limiting to protein synthesis, in which case competition for a common pool of ribosomes by mRNAs can lead to cross-talk when large systematic changes in ribosome levels occur.[15,16] In yeast, competition of a limited supply of translation machinery between mRNAs associated with galactose network creates a threshold capacity for protein synthesis that controls cell decision to divide or not.[17] Whether DTP cells, as a slow-cycling population, employ a mechanism to adjust their pool of available ribosomes and potentially transition into stress-induced cell state, has yet to be explored.

Mathematical modeling has been extensively used in many areas of cancer research, including disease initiation, progression, and treatment.[18,19] Likewise, previous research has integrated mathematical models to investigate the transition of cancer cells into a persister cell state.[20] By incorporating birth-death parameters and deterministic phenotypic switching, researchers quantified the transition rate to the persister cell state using a modified Luria-Delbrück fluctuation assay, which demonstrated a Poisson distribution of cell abundance under chemotherapy. This suggests that the transition from sensitive cells to persister cells induced by chemotherapy may be the predominant pathway for developing tolerance to SOC treatments in colorectal cancers. However, this phenotypic model does not include any mechanistic insights at the cellular level. Similar phenotypic modeling has also been utilized previously to reveal the dynamics between parental, persister, and resistant cells in a non-small cell lung cancer model.[21] An individual-based model with an integro-differential equation was used to formulate the reversible phenotypic evolution of persister cells upon EGFR inhibition. The researchers showed that the speed of adaptation depends on the cellular microenvironment, the level of survival potential, and the average sensitivity of the cell proliferation rate to the treatment at any given time. However, the biological mechanisms underlying this adaptation speed remains unclear. Recently, the advent of multi-omics has provided large, multivariable datasets, helping to formalize correlations, expression signatures, and cell connectivity using statistical modeling. However, these methods generally lack the ability to define causality or measure parameters controlling cellular phenotypes. Integrating biological insights with mathematically based computational methods has the potential to bridge this gap, leveraging a wide array of analytical tools to focus on cellular mechanisms and make precise temporal predictions. In addition, iterating *in silico* experiments in combination with model prediction validation in the wet lab can further advance model predictability and reveal underlying biological mechanisms that may not be evident in experimental settings.

In the present study, we developed a mathematical framework based on biological insights to uncover the potential impact of limited ribosome levels in DTP cells. By combining *in vivo* and *in vitro* data and computational modeling, we showed that setting ribosome level thresholds in DTP cells creates competition among mRNAs. Some are favored in treatment-naïve cells, while others thrive in DTP cells, leading to a ribosome-induced survival checkpoint that we termed "Risk." This conceptual framework unveils a potential therapeutic opportunity, supported by our mathematical framework for optimizing interventions against DTP cancer cells.

RESULTS

Reduced ribosome levels in DTP cells across various cancer types

We previously demonstrated a global reduction in mRNA translation in melanoma DTP cells, which is associated with significant m6A-related mRNA translation remodeling when treated with BRAF/MEK inhibitors (BRAFi/MEKi). The m6A modification within the 5′-UTR and 3′-UTR of specific mRNAs was revealed to facilitate selective mRNA translation in response to drug treatment in melanoma DTP cells.[7] We extended this translational regulation phenomenon to other cancer types and treatment strategies. We found that, similar to BRAFV600E-mutated A375 melanoma cells treated with BRAFi/MEKi (Figure 1A), $EGFR^{del19}$-mutated lung adenocarcinoma PC9 cell line exhibited a substantial global reduction in translation activity, as detected through polysome profiling following EGFR inhibitor treatment (erlotinib) (Figure 1B). PC9 persister cells demonstrated a lower content of polysome-bound mRNAs compared to their parental cells, as observed through ultracentrifugation on a sucrose gradient. Similar results were also noted in cholangiocarcinoma QBC939 persister cells treated with chemotherapy combo (gemcitabine and cisplatin) (Figure 1C). The global reduction in translation activity in various DTP cells, including human BRAFV600E mutant melanoma cell WM793, human cholangiocarcinoma cell RBE, mouse melanoma cell lines (YUMM1.7 and YUMM2.1) (Figure S1A), coincides with a decrease in the expression of key translation regulators like c-Myc, as well as ribosomal proteins such as RPS6, RPL7, and RPS15 (Figure 1D). We then investigated whether the reduced expression of ribosomal proteins could be observed *in vivo* and in patient samples. To address this, we examined gene expression profiles of ribosomal protein alterations in longitudinal samples from a murine melanoma model[22] treated with BRAFi (vemurafenib) (YUMM1.7 *Braf/Pten/Cdkn2a*-mutatnt cells subcutaneously transplanted into C57BL/6 mice). We analyzed transcriptomes from vehicle-treated tumors (Figure 1E, vehicle), tumors during the regressing phase (Figure 1E, regression), on-treatment tumors at the residual phase (Figure 1E, residual), and regrowing tumors under continued targeted therapy (Figure 1E, progression). Our results demonstrated higher expression of ribosomal proteins in vehicle-treated tumors (Figure 1F, violet). Treatment with vemurafenib induced a downregulation of ribosomal protein expression during the regression phase, and this reduction was further

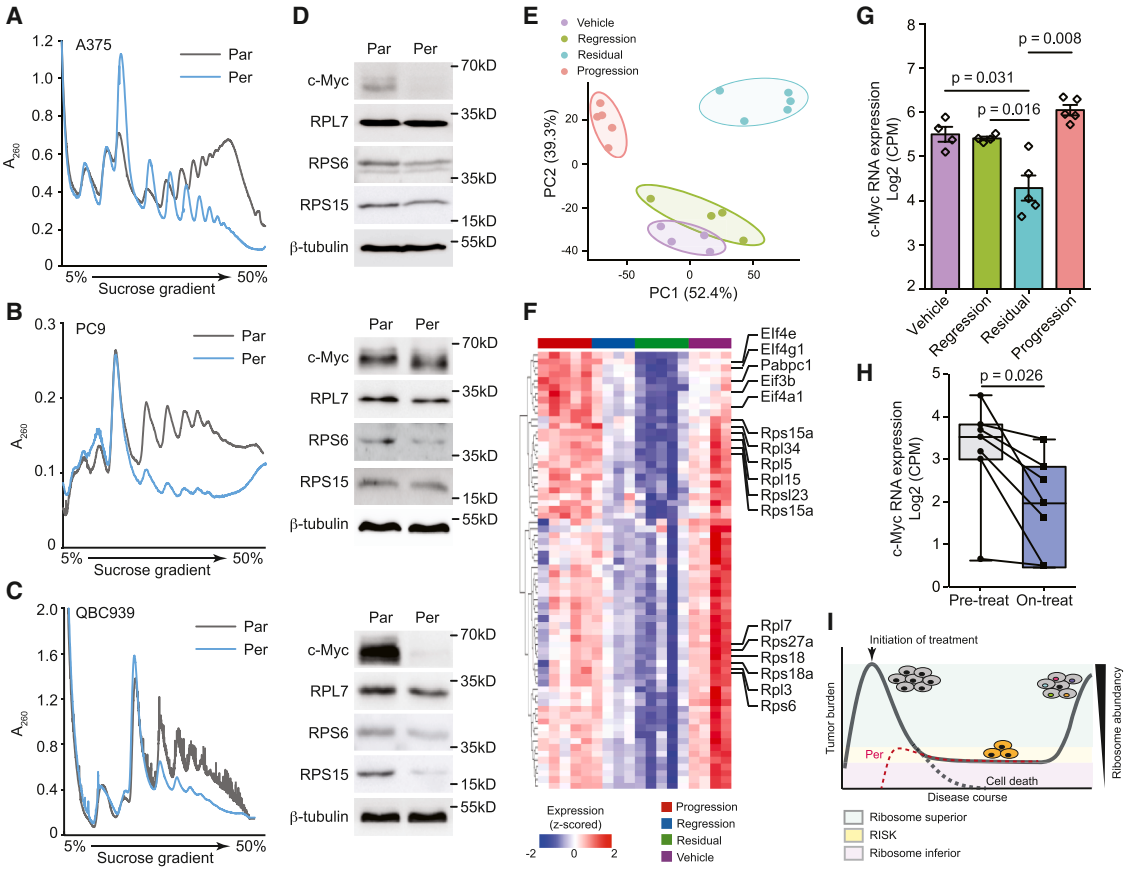

Figure 1. Decreased ribosome levels observed in DTP cells across different types of cancer

(A–C) Polysome profiles of DTP cells across various cancer types and treatment regimens. A375 BRAF^{V600E} melanoma cells were treated with vemurafenib (1 μM) and cobimetinib (500 nM) for 3 days; PC9 EGFR^{del19} lung adenocarcinoma cells were treated with 1 μM erlotinib for 5 days; QBC939 cholangiocarcinoma treated with 10 μM gemcitabine and 5 μM cisplatin, evaluated using sucrose-gradient ultracentrifugation with a range of 5% to 50%. Par: parental cells subjected to dimethyl sulfoxide (DMSO) treatment, Per: persister cells. All the polysome profiling in each cell model have been performed in n = 3 biological independent experiments, representative profiling images were shown here.

(D) Western blotting analysis of key translation regulator c-Myc and ribosomal proteins in different type of cancer DTP cells. β-tubulin was used as a loading control. Representative results were shown, all blots in each cell model were performed in n = 3 independent biological experiments.

See also Figure S1A.

(E) Principal-component analysis of the transcriptomic data from four different treatment phases, including untreated samples, regression phase, stable residual phase, and regrowth phase. n = 4 independent mice were analyzed in each group.

(F) Transcriptomes analysis of ribosomal proteins alterations of a murine melanoma model at various phases.

(G) Transcriptional changes of c-Myc expression in murine melanoma model.[22] Data are shown as mean ± SD (n = 4 mice). The Mann-Whitney nonparametric t test p values were calculated.

(H) The mRNA expression level of c-Myc within biopsies from melanoma patients treated with vemurafenib.[23] Data are shown as mean ± SD from n = 7 paired melanoma patient samples in pre-treatment and on-treatment samples. The Mann-Whitney nonparametric t test p values were calculated.

See also Figure S1.

(I) Schematic view of the dynamics of treatment response in relationship with persister cells.

pronounced at the residual phase (Figure 1F). However, ribosomal protein expression rebounded to a level comparable to that of vehicle-treated tumors when murine melanoma regrew under continued targeted therapy (Figure 1F). These *in vivo* findings align with the *in vitro* observation of a global downregulation of ribosomal protein expression and translation activity in DTP cells across different cancer types and treatment regimens (Figures 1A–1D). Given that c-Myc has been identified as a direct regulator of ribosome production and plays a role in coordinating mRNA translation through the transcriptional control of RNA and protein components of ribosomes,[24] we observed a similar trend of transcriptional alteration in *Myc* expression as noted for the ribosomal protein expression during the treatment of BRAFi in murine melanoma model (Figure 1G). Gene set enrichment analysis (GSEA) analysis showed specific downregulation of Myc target genes during residual phase in melanoma mouse models (Figures S1B and S1C). The reduced expression of c-Myc during the residual phase of targeted therapy was further confirmed in transcriptomic dataset[23] from biopsies of melanoma patients treated with BRAFi (Figure 1H). In response to the initial systemic

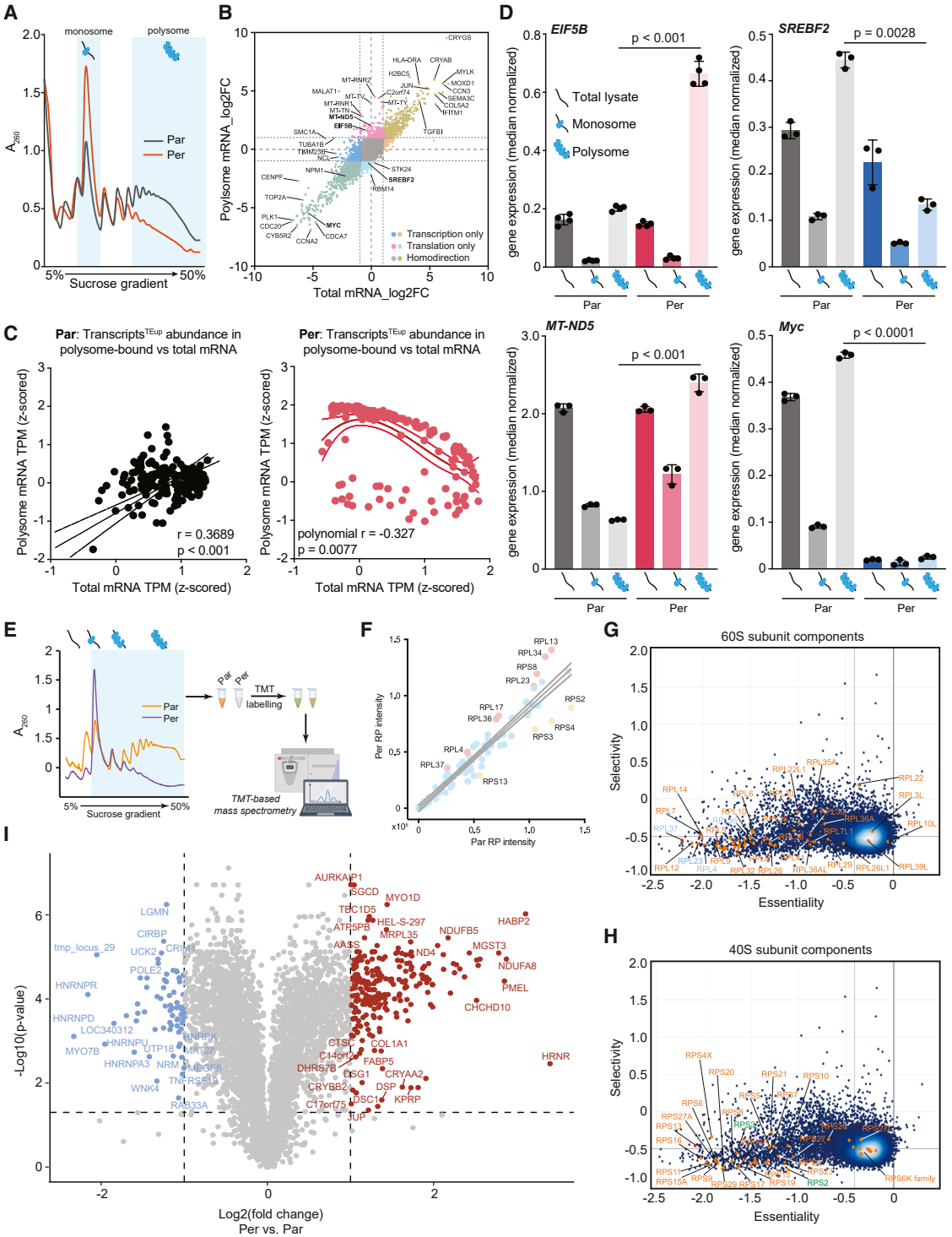

Figure 2. Translational alterations and specific ribosomes associate with the essentiality of ribosomal proteins in DTP cells

(A) Polysome profile of A375 human melanoma cells whose mRNAs were subjected to polysome RNA-seq.

See also Table S1.

(B) Scatterplot of genome-wide transcripts undergoing differential regulation at transcription and translation level. Total mRNAs (transcription) and polysome-bound mRNAs (translatome) were analyzed by using Xtail software, the respective transcripts were classified into three categories, including transcriptional regulation (|total mRNA $\log_2$fold change| > 1, polysome mRNA $\log_2$fold change| < 1, *p*-adjusted <0.05), translational regulation (|total mRNA $\log_2$fold change| < 1, polysome mRNA $\log_2$fold change| > 1, *p*-adjusted <0.05) and homodirectional regulation.

(legend continued on next page)

treatment, a small subset of tumor cells enters a temporary state of persistence (Per), which enables residual tumor cells to survive until more permanent mechanisms of resistance can be established (Figure 1I). In this context, DTP cells must contend with limited ribosome levels, and their survival hinges on robust strategies governing the allocation of these persistence-associated ribosomes to the myriad cellular processes. This situation may potentially lead to a "Risk"-associated bottleneck effect in ribosome levels, serving as a checkpoint for the survival and growth of DTP cells.

Selective translation under global translational repression in DTP cells

To characterize selective translation in DTP cells, we performed polysome-profiling-based RNA sequencing (polysome RNA sequencing [RNA-seq]) in A375 parental and DTP cells (Figure 2A). Total mRNA (transcriptome) and polysome-associated mRNA (translatome) were analyzed in parallel. By comparing fold-changes in total versus polysome-bound mRNAs, transcripts were classified as transcriptionally altered, translationally altered, or homodirectionally altered (Figure 2B). Consistent with prior observations, homodirectionally downregulated transcripts were enriched for cell-cycle and transcriptional regulators (e.g., PLK1, CDC20, CCNA2, and CENPF). Homodirectionally upregulated transcripts instead included stress- and Epithelial-mesenchymal transition (EMT)-associated genes such as IFITM1, COL5A2, TGFBI, JUN, and SEMA3C. Key regulators of ribosome biogenesis (MYC and NPM1) were also reduced in DTPs, indicative of a global decrease in translational capacity (Figure 2B).

We identified 193 transcripts whose polysome association increased despite unchanged total mRNA levels (Figure 2B, pink; Table S1). Pathway analysis revealed significant enrichment for mitochondrial translation and oxidative phosphorylation components (Figure S2A), including MT-ND5, MT-TN, and MT-RNR2 (Figure 2B). We next examined the relationship between mRNA abundance and translation for these selectively translated transcripts (hereafter Transcript^{TEup}). In parental cells, transcript and polysome-bound mRNA levels were positively correlated (Figure 2C, left). In contrast, DTP cells showed a marked dissociation between transcription and translation, with several transcripts exhibiting high polysome occupancy despite lower mRNA abundance (Figure 2C, right). These observations suggest a state-dependent shift toward non-linear, selective translation in DTPs. We validated representative transcripts by qPCR of total, monosome, and polysome fractions (Figure 2D). EIF5B and MT-ND5 showed increased polysome association without corresponding changes in total mRNA, whereas SREBF2 was selectively reduced at the translational level. MYC was concordantly downregulated in both total and polysome fractions. At a genome-wide level, Transcript^{TEup} genes exhibited shorter transcript and 5′-UTR lengths and higher guanine-cytosine (GC) content compared with other transcripts (Figure S2B), suggesting that intrinsic mRNA features may contribute to their preferential translation.

To assess these findings in independent models, we performed analogous polysome RNA-seq in the YUMM1.7 mouse melanoma model (Figures S2C–S2H and Table S1). Although specific transcripts differed between species (Figure S2D), several regulators—including Eif5b, Myc, Npm1, and Srebf2—showed similar patterns of alteration. Mitochondrial translation was again enriched among selectively translated genes (Figure S2G). As in A375 cells, transcription-translation coupling was maintained in Transcript^{TEup} of parental cells but uncoupled in DTPs (Figure S2E). The qPCR validation of selected transcripts reproduced the observed patterns (Figure S2F). Transcript^{TEup} genes in the mouse model also shared shorter transcript and 5′-UTR lengths and increased GC content (Figure S2H).

Ribosome component alterations in DTP cells associate with RP essentiality

Upon the observation of downregulation of ribosome abundance in multiple cancer persistence models and selective translation in two cell models from distinct species, we tried to understand the regulatory mechanisms underlying the generation of "Risk" in DTP cells. We firstly employed quantitative high-coverage tandem-mass-tag (TMT) mass spectrometry[25,26] in human melanoma DTP cells and treatment-naïve parental cells to measure the expression of all ribosomal proteins (Figure S3A and

See also Figure S2.

(C) The correlation between total mRNA and polysome-bound mRNA abundance of transcripts selectively upregulated at the translational level in persister cells (Transcript^{TEup}). Left, the respective abundances of Transcript^{TEup} genes in total mRNA and polysome-bound mRNA fractions in A375 parental cells (Par); Right, the respective abundances of Transcript^{TEup} genes in total mRNA and polysome-bound mRNA fractions in A375 persister cells (Per). $N = 4$ independent biological samples were analyzed in each fraction.

See also Figure S2.

(D) Quantitative PCR examination of corresponding transcripts in different fractions of A375 cells, including total mRNA fraction, 80S monosome and polysome fractions. Unpaired *t* test was performed for statistical analysis.

See also Figure S2.

(E) Schematic view of quantitative high-coverage tandem-mass-tag (TMT) mass spectrometry measuring the expression of all ribosomal proteins within parental (Par) and DTP cells (Per).

(F) TMT-mass spectrometry-based comparative analysis of ribosomal protein components in parental (Par) and DTP cells (Per). $N = 2$ biological independent samples were analyzed in TMT experiment.

See also Figure S3.

(G and H) Essentiality analysis of ribosomal proteins derived from DTP cells based on The Cancer Dependency Map (DepMap) project.

(G) Upregulated propensity of ribosome proteins (RPs) within large subunit.

(H) Downregulated propensity of RPs within small subunit.

(I) Differential expression analysis of ribosome-bound proteins in parental (Par) and DTP cells (Per) based on TMT mass spectrometry. Red dots, fold change >2, adjusted p value <0.01; Blue dots, fold change <2, adjusted p value <0.01.

See also Table S2.

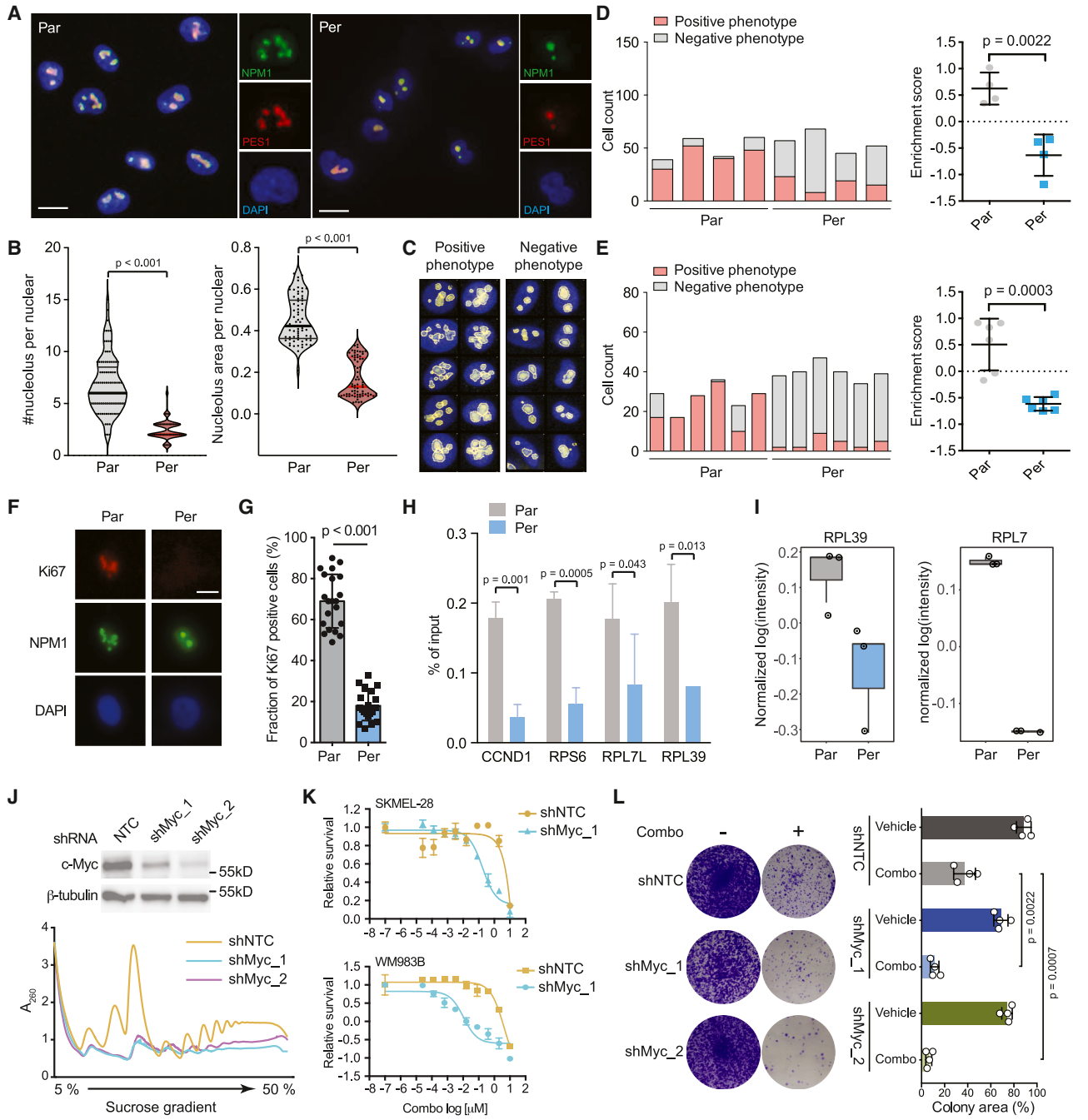

Figure 3. Myc-mediated downregulation of ribosome biogenesis in DTP cells

(A) Immunofluorescence of nucleolar proteins, nucleophosmin 1(NPM1, green) and pescadillo (PES1, red), showing different phenotype of ribosome biogenesis center in parental and DTP cells. Representative images were shown from $n = 3$ biological independent experiments. Scale bars, 10 μm.

(B) Quantification of nucleolus number and area per nuclear at single cell level in A375 melanoma cells. Four different regions of interest were randomly selected for image analysis, and a total of 100 cells were analyzed. Unpaired *t* test Mann-Whitney test was performed for statistical analyses.

(C) Image-based machine learning classification by using Cellprofiler[34] to categorize the nucleolar phenotype into positive (more number and higher granularity) and negative (less number and lower granularity) feature.

(D and E) The nucleoli of DTP cells exhibited a higher proportion of negative features in two distinct DTP models.

(D) A375 melanoma persister cells treated with 1 μM vemurafenib and 500 nM cobimetinib, $n = 4$ different regions of interest were randomly selected for image analysis, and a total of 100 cells were analyzed.

(E) Lung adenocarcinoma PC9 persister cells treated with 1 μM erlotinib. $N = 6$ different regions of interest were randomly selected for image analysis, and a total of 100 cells were analyzed. Data are shown as mean ± SD. The Mann-Whitney nonparametric *t* test *p* values were calculated.

(legend continued on next page)

Table S2). We fractionated parental and DTP cells by sucrose gradient sedimentation and collected 80S ribosomes (a single ribosome) and polyribosomes (≥2 ribosomes) to isolate active translating ribosome-associated proteins[27] (Figure 2E). The TMT labeling, by adding a unique chemical tag to the peptides, allowed us to quantify the relative RP abundance in each cell state. On average, we detected peptides predominantly in the range of 10–30 amino acids, with a high protein coverage (Figures S3B–S3E). A diverse array of subcellular proteins potentially associated with polysomes was detected, with a substantial proportion belonging to mitochondrion proteins (39.77%) (Figure S3F). GSEA analysis showed an enrichment of ribosome biogenesis-related components that is downregulated in DTP cells in our mass spectrometry analysis. In addition, TMT mass spectrometry showed downregulation of cell cycle-related peptides in DTP cells that is consistent with their slow-cycling phenotype (Figure S3G).

In parental and DTP cells, the majority of RPs remains unchanged. However, we observed increased usage of RPs within ribosome large subunit in DTP cells compared to parental cells, such as RPL37, RPL4, RPL36, and RPL23 (Figure 2F). In contrast, decreased abundance of RPs within ribosome small subunit was observed in DTP cells, such as RPS3, RPS2, RPS13, and RPS4 (Figure 2F). The alteration of ribosome component is seemly associated with gene essentiality across myriad cell types, whose loss of function is negatively associated with cellular survival. The Cancer Dependency map (DepMap) project has performed genome-wide CRISPR-Cas9 screening of cultured cell lines to interrogate the dependency of individual genes in different cell types.[28] By focusing on the ribosomal proteins, we observed that those upregulated propensity of RPs within ribosomes derived from DTP cells have shown strong essentiality in different cancer cell lines, including RPL4, RPL37, RPL23 (Figure 2G), whereas no such a correlation was observed for those small subunit RPs that are downregulated within ribosomes from DTP cells (Figure 2H). We noted that because sucrose gradient-based TMT mass spectrometry measures total protein levels within a given ribosome-bounded fraction, we cannot exclude the possibility that the residual pool of mRNA-bounded ribosomes with variable composition could result in ribosome stalling during the elongation,[29] thus leading to global downregulation of translation activity in DTP cells (Figures 1A–1C). We further exploited the ribosome transit rate on an mRNA population by using a harringtonine run-off assay in parental and DTP cells.[30] The translation inhibitor harringtonine stalls initiating ribosomes at the start codon while allowing already initiated ribosomes to continue elongating and run off their binding mRNAs (Figure S4A); thus, the time it takes for polysome depletion after harringtonine treatment correlates with translation elongation speed.[31] Treatment of harringtonine resulted in a reduction of polysomes and a dramatic increase in 80S monosomes in both parental and DTP cells (Figure S4B), suggesting that there is no basal level of ribosome collisions within the two cell states. On the contrary, the downregulation of ribosome levels and Myc expression observed in *in vivo* and patient samples were consistent with the differential expression analysis of TMT mass spectrometry dataset. We observed a downregulation of peptide abundances derived from heterogeneous nuclear ribonucleoproteins (hnRNPs) that are potentially involved in pre-mRNA processing and ribosomal RNA (rRNA)-associated ribosome biogenesis,[32] such as HNRNPR and HNRNPD (Figures 2I and S3G). Whereas, increased expression of ribosome-bounded peptides, such as mitochondrial proteins (ND4 and NDUFA8) and fatty acid binding proteins (FABP5), was observed in DTP cells, which is consistent with our previous study showing increased mitochondrial metabolism within melanoma DTP cells.[33] Taken together, reduced level of ribosome proteins did not result in dramatic alterations of ribosome components and downregulation of global translation activity was not due to ribosome collision on their transcripts in DTP cells.

Myc-dependent reduction of ribosome biogenesis in DTP cells

Since our systematic mass spectrometry analysis suggested that ribosome biogenesis may be mitigated in DTP cells, we subsequently exploited the underlying mechanisms that regulate the ribosome production in DTP cells. Ribosome biogenesis is a highly dynamic and energy consuming process, in which rRNA is synthesized, modified, and assembled with RPs to form mature ribosomes. Ribosome biogenesis takes place within specialized subnuclear compartments known as the nucleoli.[24] We stained cells with two nucleolar markers, including nucleophosmin 1(NPM1) and pescadillo (PES1), in parental and DTP cells (Figure 3A). NPM1 located primarily in the granular regions of the nucleolus, and interaction with PES1 is required for ribosome biogenesis and genomic stability

(F and G) Lower intensity of cell proliferation marker Ki67 staining showing correlation with negative feature of nucleolar phenotype in A375 melanoma DTP cells. Representative images were shown from $n = 3$ biologically independent experiments. Ki67 fluorescence intensity was quantified within individual cells ($n = 30$) by Cellprofiler software.[34] The Mann-Whitney nonparametric *t* test *p* values were calculated.

(H) Chromatin immunoprecipitation (ChIP) with c-Myc antibody in A375 melanoma parental (Par) and DTP cells (Per). Genomic DNA was purified and quantitative PCR was conducted to assess the enrichment levels of the corresponding c-Myc binding sequence. The data are presented as the mean ± SD from $n = 3$ biologically independent experiments. CCND1 enrichment level was used as a positive control. The Mann-Whitney nonparametric *t* test *p* values were calculated.

(I) Levels of RPL7L and RPL39 proteins were downregulated in DTP cells compared to parental cells, as indicated by TMT mass spectrometry analysis. Data are shown as mean ± SD. The Mann-Whitney nonparametric *t* test *p* values were calculated.

(J) Knockdown of c-Myc reduced global translational activity in A375 melanoma cells as indicated by polysome profiling. Inset, c-Myc shRNA analysis by western blot. $n = 3$ biologically independent experiments were performed showing similar results.

(K) Knockdown of c-Myc enhanced the responsiveness to vemurafenib and cobimetinib treatment in SK-MEL-28 and WM983B melanoma cells. Representative results were shown from $n = 3$ biologically independent experiments. Data are shown as mean ± SD.

(L) Clonogenic assay of A375 melanoma cells under vemurafenib and cobimetinib treatment with or without c-Myc shRNA-mediated knockdown for 3 weeks. $N = 4$ biologically independent experiments were performed. Data are shown as mean ± SD. The Mann-Whitney nonparametric *t* test *p* values were calculated. Corresponding clonogenic assay example images were shown for each treatment group. Combo, vemurafenib (1 μM) + cobimetinib (500 nM).

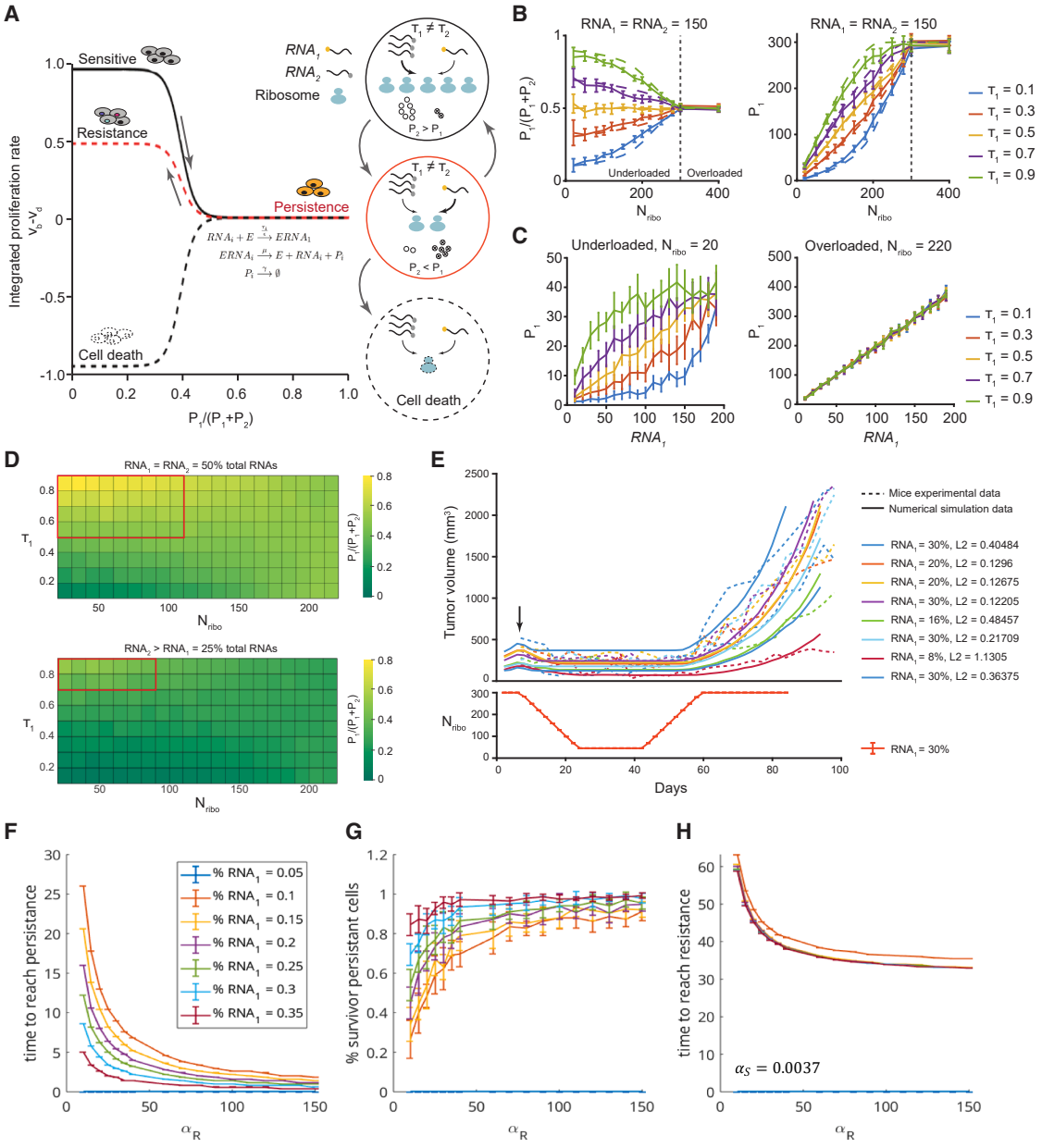

Figure 4. Mathematical framework of ribosome-induced survival checkpoint (RISK)

(A) The "Risk" model description. RNA_i (i = 1 or 2), RNA_1 represents stress-related genes featuring increased N6-methyladenosine modification in their 5′UTR (yellow dot on the mRNA), RNA_2 represents proliferation-related genes featuring increased N6-methyladenosine modification in the 3′UTR (gray dot on the mRNA); P_i (i = 1 or 2), corresponding protein productions of RNA_i; E = N_R, an ensemble of ribosomes; μ, production rate of proteins; γ, degradation rate of proteins; τ_i (i = 1 or 2), the ribosome interaction preference weight of each type of mRNA.

(B and C) Mathematical model exploration of the relationship between mRNA and protein production in ribosome overloaded or under loaded conditions.

(B) $RNA_1 = RNA_2 = 150$. From left to right: mean ratio of P_1 to total protein at equilibrium, mean number of P_1 as function of the abundance of ribosomes N_{ribo}. Continuous lines, result of the simulation. Dotted line, approximated mean by *Wallenius* noncentral hypergeometric distribution.

(C) From left to right: $N_{ribo} = 20$ (underloaded), $N_{ribo} = 220$ (overloaded). Mean number of P_1 as function of RNA_1 for different values of τ_1: $\tau_1 = 0.1$ (blue curve), $\tau_1 = 0.3$ (red curve), $\tau_1 = 0.5$ (yellow curve), $\tau_1 = 0.7$ (purple curve), $\tau_1 = 0.9$ (green curve).

See also Figure S5.

(D) Protein production allocation under differential ribosome quantities. From top to bottom: $RNA_1 = RNA_2 = 50\%$ total RNAs, $RNA_2 > RNA_1 = 25\%$ total RNAs. Functional relationship of τ_1, N_{ribo} and resulting ratio of P_1 to total protein at equilibrium. Darkness or lightness of the square color represents the relative protein ratio of P_1 to total protein.

(legend continued on next page)

control.[35] We found that less number and lower total area of nucleoli per nuclear was shown in DTP cells compared to parental cells (Figure 3B). To integrate the heterogeneous phenotypes of nucleoli observed in parental and DTP cells, we developed an image-based machine learning classification method by using Cellprofiler[34] and trained the nucleolar phenotype into positive and negative feature (Figure 3C). We found that DTP cell's nucleoli showed higher fractions of negative feature in two different DTP models, including A375 melanoma persister cells treated with BRAFi/MEKi (Figure 3D) and lung adenocarcinoma PC9 persister cells treated with EGFRi (Figure 3E). In addition, NPM1 negative phenotypic DTP cells showed decreased intensity of Ki67 staining, suggesting that these cells are undergoing a slow-cycling or quiescent transition (Figures 3F and 3G).

Myc binds to sequences both upstream and downstream of the coding regions within ribosomal DNA clusters, exerting direct control over the RNA polymerase I-dependent transcription of 18S, 5.8S, and 28S rRNAs.[36] Given that c-Myc expression alterations showed similar trend comparable to ribosomal proteins, we exploited Myc-mediated transcriptional regulation of ribosomal proteins through chromatin immunoprecipitation of c-Myc followed by quantitative polymerase chain reaction (qPCR) for RPs. As shown in Figure 3H, the binding of c-Myc to the promoters of ribosomal genes, such as RPS6, RPL7L, and RPL39, were decreased in DTP cells compared to that of parental cells. In consistence with downregulation of Ki67 expression, the recruitment of c-Myc to the promoter of cyclin D1 (CCND1) was also diminished (Figure 3H). The expressions of RPL7L and RPL39 proteins were also downregulated in DTP cells compared to that of parental cells as shown by TMT mass spectrometry (Figure 3I).

The knockdown of c-Myc *per se* significantly reduced global translation activity in SK-MEL-28 melanoma cells (Figure 3J), potentially resetting the threshold of ribosome abundance and the adaptive capacity within DTP cells. In line with this, our findings indicate that c-Myc knockdown enhances the responsiveness to combo treatment (BRAFi/MEKi) across different melanoma cells (Figure 3K). This implies that disrupting ribosome biogenesis by inhibiting the master regulator c-Myc may potentially alleviate the generation of DTP cells during drug treatment. The clonogenic assay, conducted in the presence of BRAFi/MEKi treatment with or without c-Myc knockdown, further validated these results (Figure 3L). Taken together, these data suggest that the transactivation of ribosomal genes mediated by c-Myc is downregulated in DTP cells, resulting in decreased ribosome biogenesis. This reduction in ribosome production may establish a ribosome-level threshold, potentially serving as a checkpoint for selective mRNA translation.

Queuing theory model for ribosome-mediated mRNA competition

To investigate how DTP populations evolve under differing levels of ribosome availability—high in rapidly proliferating, treatment-naïve cells, and low in slow-cycling DTPs—we developed a mathematical model that links ribosome abundance to cell-state transitions. The model incorporates a ribosome-dependent "survival checkpoint" (Risk), which determines whether cells remain proliferative, enter a DTP state, or progress toward stable resistance. In this framework, each cell contains two classes of mRNAs that compete for access to a finite ribosome pool. Because ribosomes are limited, changes in their availability disproportionately affect the translation of different mRNA species, thereby shifting the production of the proteins that determine cell state. Thus, ribosome scarcity or abundance becomes a central driver of cell-state decisions.

The translation-competition module of the model is built on queuing theory,[37] an analytical approach originally designed to manage constrained resources in engineering systems such as telecommunications, manufacturing, and computer networks. Queuing theory is particularly appropriate here because it classifies system behavior according to whether it operates in an overloaded or underloaded regime.[38] Applied to translation, these regimes correspond to conditions where ribosomes are either saturated by mRNA demand or available in excess, providing a natural mathematical language to describe how cells shift between proliferative, persister, and resistant states. This modeling strategy therefore offers an intuitive and quantitative framework for understanding how ribosome availability governs DTP dynamics during therapy.

Figure 4A summarizes the dynamics of the "Risk" model (Method S1). Each cell contains two classes of mRNAs (RNA1 and RNA2) that compete for a shared pool of N_R ribosomes (E). Ribosome binding generates translation complexes $ERNAi$ (i = 1 or 2), ultimately producing two corresponding proteins, P1 and P2. Each mRNA species is assigned a ribosome-interaction preference τ_i (i = 1 or 2), reflecting our earlier findings that distinct m^{6}A modification patterns confer differential translational efficiency[7] (Figure 4A inset formula and Method S1). Protein production and degradation are modeled as Poisson processes with rates μ and γ, respectively. The reactions are summarized as follows:

$$mRNA_i + E \xrightarrow{\frac{\tau_i}{\varepsilon}} ERNA_i$$

$$ERNA_i \xrightarrow{\mu} E + mRNA_i + P_i$$

$$P_i \xrightarrow{\gamma} \varnothing.$$

(E) Parameter estimation of mathematical model by using experimental data from *in vivo* A375 melanoma xenograft. Top: evolution of the number of melanoma cells in continuous 200 ppm PLX4720 (BRAFi) and 7 ppm PD0325901 treatment for different initial conditions of %RNA$_1$. Dotted lines represent experimental data. Continuous lines represent computational simulated results. Bottom: the corresponding dynamic changes in N_{ribo} over days.
(F–H) Evolution of time to reach persistence revealed by the mathematical model, for α_S = 0.0037.
(F) The time to reach persistence as a function of ribosome adaptation speed α_R under different initial percentage of RNA$_1$.
(G) The corresponding percentage residual persister cells.
(H) The time to reach acquired resistance as a function of ribosome adaptation speed α_R.
See also Figure S6.

We then consider the limiting case as $\varepsilon \to 0$, which corresponds to an instantaneous interaction between ribosomes and available mRNA transcripts. In this regime, any free ribosome is assumed to bind immediately to an mRNA within the pool.

Using Markov chain theory (see Method S1), our model reveals two distinct regimes of protein production dictated by ribosome availability. When ribosomes are abundant relative to total mRNA (overloaded scenario), the fraction of each protein is proportional to the corresponding mRNA abundance (Figures 4B, 4C, and S5A–S5C). In contrast, when ribosomes are limiting (underloaded scenario), protein fractions depend nonlinearly on mRNA abundance, with the relationship strongly influenced by the translational preference weight τ_1 (Figures 4B, 4C, S5A, S5B, and S5D). Figure 4D illustrates the fraction of P1 as a function of ribosome number (N_R, *x* axis) and τ_1 (*y* axis) for mRNA1 constituting 50% or 25% of the total mRNA pool (top and bottom images, respectively). This result showed that mRNAs with high translational preference are efficiently translated even at low ribosome concentrations, whereas mRNAs with low preference become poor substrates under ribosome-limiting conditions, regardless of their abundance (Figure 4D). Thus, the "Risk" model predicts that a cell's predominant protein output can shift with ribosome availability, driven by selective suppression of mRNAs with intrinsically low translational efficiency (Method S1).

Mathematical analysis of persistence-associated cell states

Incorporating this translational regulatory mechanism, the "Risk" framework defines four potential states for drug-treated cancer cells: (1) proliferative, drug-sensitive cells (sensitive); (2) slow-cycling DTPs (persistence); (3) regrown, drug-resistant cells (resistance); and (4) cell death (Figure 4A). Transitions among these states are governed by two key factors: (1) the relative proportion of proteins produced, with P1 promoting survival under stress (persistence) and P2 supporting proliferation (sensitive and resistance); and (2) a model variable capturing acquired resistance during prolonged treatment (resistance). Specifically, given the fraction of P2 relative to total protein $\frac{P_2}{P_1+P_2}$ the cell's proliferation rate (ν_b) and death rate (ν_d) are defined as

$$\nu_b\left(\frac{P_2}{P_1+P_2}\right) = \nu_b^*\psi_h\left(\frac{P_2}{P_1+P_2}\right),$$

$$\nu_d\left(\frac{P_2}{P_1+P_2}\right) = c(t)\,\nu_d^*\psi_h\left(\frac{P_2}{P_1+P_2}\right),$$

here $c(t)\in[0,1]$ represents binary environmental stress parameter (e.g., $c(t) = 1$ during drug treatment and $c(t) = 0$ in its absence), and $\psi_h(r)$ is a sigmoid function (Method S1) commonly used to capture key tumor growth dynamics: initial exponential expansion, deceleration under resource limitation, and plateau at carrying capacity, which is standard in modeling tumor responses to therapy.[39] Under this framework, cells producing predominantly P2 proteins not only proliferate at the maximal rate ν_b^*, but also experience a death rate ν_d^* under treatment (sensitive state, $\nu_d^* > \nu_b^*$), whereas cells producing mainly P1 proteins neither proliferate nor die under drug exposure (persistence state). The transition between these states is triggered by a linear decrease in ribosome abundance during treatment, which is consistent with experimental systems such as cancer cells treated with chemotherapeutic drugs,[40] model organisms,[41] and neuroepithelial differentiation,[42] all of which exhibit monotonic decreases in ribosome levels. Western blot analysis of ribosomal proteins, including RPS15, RPS6, and RPL7, confirmed that their levels decrease linearly over time in the context of DTPs (Figures S5E and S5F). This ribosome reduction may create a translational bottleneck, shifting protein production toward the preferred transcript (P1) and establishing the persister state.

To model resistance acquisition, we allow the maximal death rate parameter ν_d^* to evolve during treatment

$$\frac{d\nu_d^*}{dt} = \begin{cases} -c(t)\alpha_s\left(1 - \psi_h\left(\frac{P_2}{P_1+P_2}\right)\right) & \text{if } c(t) > 0 \\ \alpha_d\,\frac{\nu_d^*}{\nu_0}\,1\left(\nu_d^* > \bar{\nu}\right), & \text{if } c(t) = 0 \end{cases}$$

provided with the condition $\nu_d^* \in [0, \nu_0]$, and initial condition $\nu_d^*(0) = \nu_0 > \nu_b^*$ (all parental cells are equally sensitive to the treatment). Thus, persister cells gradually lose sensitivity at a constant rate α_s during exposure and regain sensitivity exponentially ($\frac{\alpha_d}{\nu_0}$) once the drug is removed, until reaching an irreversible resistant state characterized by restored proliferation and translation activity comparable to parental cells ($\nu_d^* < \bar{\nu}$). Ribosome dynamics in resistant cells are described using a classical protein production-degradation model

$$\frac{dN_R}{dt} = f\left(c(t), \nu_d^*\right)\alpha_R.$$

Here $N_{R,min} < N_R < N_{R,max}$, with f (c(t), v_d^*) representing ribosome synthesis and decay contingent on perceived drug concentration expressed as

$$f\left(s, \nu_d^*\right) = \begin{cases} 1 & \text{if } s = 0 \text{ or } \nu_d^* > \bar{\nu}\ (\text{no drug or resistant}) \\ -1 & \text{otherwise}. \end{cases}$$

All model parameters and initial conditions are summarized in Method S1.

Sensitivity analysis and experimental evaluation of the "Risk" framework

To streamline the model, we quantified how each parameter influences system behavior across experimentally grounded conditions. Guided by our earlier translational (Figures 4B–4D), we fixed a high translational preference weight $\tau_1 = 0.9$ for RNA_1 and initialized cells with a defined ribosome pool to $N_R = 30$in all simulations. Under continuous treatment (for $c(t) \equiv 1$) and starting from a fully sensitive population ($> \nu_b^*$), we evaluated how remaining parameters shape three key readouts: time to persistence t_p, fraction of DTPs, and time to resistance t_R, capturing the clinically relevant phases of tumor regression, minimal residual disease, and regrowth.

We first focused on three parameters—ribosome adaptation speed (α_R), the fraction of persistence-linked RNA1, and the resistance rate (α_S)—while holding all others constant (Figures 4F–4H and S6). RNA1 level emerged as the dominant

driver: populations with <5% RNA1 failed to enter persistence under any α_R, whereas those with >5% RNA1 consistently reached the persistence state and did so faster as RNA1 increased, generating larger persister pools and earlier resistance. Faster ribosome adaptation amplified these effects by promoting persistence entry and accelerating resistance. In contrast, α_S acted specifically on the resistance transition: higher α_S shortened the time to resistance but did not alter persistence onset (Figures 4H and S6). We next tested whether the "Risk" model can reproduce the drug-rechallenge behavior of melanoma DTP cells *in vitro*[7] (Figure S7A). Experimentally, melanoma DTP cells remained highly tolerant to a second BRAFi/MEKi pulse when rechallenged 1–3 days after drug withdrawal, but progressively regained parental-like sensitivity after ~9 days drug-free culture (Figures S7B–S7E). Using these data, we fixed the translational parameters $\alpha_R = 30$ and $\%RNA_1 = 0.2$ to ensure persistence acquisition and exit. As mentioned before, drug response was modeled with a sigmoid function ψ_{h_s} of drug concentration by setting $c(t) = \psi_{h_s}(m_{BRAF})$, where m_{BRAF} is the BRAFi/MEKi drug concentration at time t (Figure S5F). We then examined how varying the drug response steepness h_s and death rates ν_0, ranging from 0.06 to 0.3, affected DTP levels (Figures S7G and S7H). This analysis identified $\nu_0 = 0.3$ and $h_s = 0.3$ as parameter values that best captured the observed experimental results. With these settings, the "Risk" model qualitatively recapitulated the reversible drug sensitivity of DTP populations seen *in vitro* during drug withdrawal and rechallenge (Figures S7I–S7L).

To further evaluate the validity of the Risk model, we next challenged it with *in vivo* data. Because the exact intra-tumoral drug concentration cannot be measured *in vivo*, we approximated drug exposure using a binary function, set to $c(t) \equiv 1$ during treatment periods and 0 otherwise. Continuous-treatment experiments showed emergence of persistence around day 20 and tumor regrowth around day 60 (Figure 4E), which guided the selection of parameters $\alpha_R = 15$and $\alpha_S = 0.0037$ based on our prior analysis. We first fit the *in vivo* tumor growth curves from untreated mice to estimate the proliferation rate ν_b^* and initial tumor volume (reflecting initial cell numbers). With these parameters fixed, and allowing only the proportion of RNA1 to vary across individuals (randomly sampled between 5% and 30% of total mRNA), the model robustly captured the diverse tumor growth trajectories, including resistance appearing around day 60—consistent with transcriptional heterogeneity among mice (Figure 4E). Model performance was quantified by the relative L2 error between simulated and experimental curves. We then asked whether the Risk model could recapitulate tumor dynamics under an intermittent treatment schedule (Figures S8A and S8B). Strikingly, by varying only the RNA1 proportion across individuals while keeping all other parameters constant, the model reproduced the *in vivo* kinetics observed under intermittent therapy (Figure S8C).

Computational approach to optimizing DTP cell-driven treatment

The ribosome level-induced survival checkpoint (Risk) in DTP cells may introduce vulnerability exploitable in a treatment-specific context. Within our mathematical framework, we explored two treatment strategies intervening with ribosome adaptation. Given that DTP cells rely on a minimal ribosome level for selective translation of persistence-related transcripts, direct ribosome inhibition may disrupt this process, leading to DTP cell eradication.[6] Tumor growth depends on the proliferation rate ν_d^* and cell death rate ν_0 of tumor cells, while DTP cell generation is influenced by ribosome adaptation speed α_R (Figures 4A and 5A). Prolonged drug exposure drives the evolution of DTP cells into an acquired resistant state with a resistance acquisition speed α_S. The addition of a ribosome inhibitor (RIBOi) may potentially disrupt the "Risk" balance, eliminating DTP cells and delaying the emergence of acquired resistance (Figure 5A). One of the RIBOis, homoharringtonine (HHT), was shown to bind to the A-site cleft of large subunit of 80S ribosome and thus prevent the incoming A-site tRNA from accommodating its 3′-terminal cytosine-cytosine-adenosine (CCA) end into the peptidyl transferase center (PTC).[43] HHT's translation inhibitory effect is more pronounced in eukaryotes than in archaea, making it a eukaryote-specific inhibitor. It is the only RIBOi approved for clinical use in leukemia treatment.[44]

We first explored the effect of the combination of BRAFi/MEKi and HHT treatment *in silico*. The initial cell count was estimated using experimental data from mice, as shown in Figures 4E and S8B. Additionally, we determined the value of ν_b^* through exponential fitting against the mean experimental growth curves over a 3-day time span before drug treatment. Due to the unavailability of *in vivo* data for deriving the death rate ν_0 precisely, we set it to $2^* \nu_b^*$ to achieve an 80% population loss observed in the continuous treatment. Other parameters were listed in Method S1. Vehicle and HHT monotherapy conditions were simulated *in silico* with no drug input ($c(t) \equiv 0$), whereas BRAFi/MEKi and/or HHT treatments were modeled by continuously administering the drug from day 14 onward. To assess the potential impact of ribosome adaptation on tumor evolution under drug exposure, we employed a quantitative method measuring the relative L2 error based on the trapezoidal rule between simulations and experimental data (Method S1). Figure 5B demonstrates the excellent fit of our mathematical framework, irrespective of α_R and α_S, to experimental data derived from vehicle treatment or HHT monotherapy (Figure 5B, top image). In contrast, exploring the parameter space of α_R and $\alpha_S$revealed that, under triple combination treatment (BRAFi/MEKi/HHT) for each mouse condition, L2 errors could be minimized by decreasing ribosome adaptation speed α_R at a fixed α_S. This underscores the crucial role of HHT-mediated inhibition of ribosome adaptation in the generation of DTP cells and their progression toward acquired resistance (Figure 5B, bottom, right image). However, this is not observed under BRAFi/MEKi combo treatment (Figure 5B, bottom, left image). This *in silico* exploration suggests that altering resistance acquisition speed α_S alone is insufficient to replicate the experimental data. Based on our parameter space exploration, numerical simulation aligned well with experimental data in nude mice harboring BRAFV600E-mutated A375 melanoma cells. This was achieved by fixing the ribosome adaptation rate $\alpha_R = 27$ for BRAFi/MEKi combo treatment and decreasing it to 15 for triple combination treatment, with $\alpha_S = 0.0262$ for both conditions, as shown in Figure 5C in which solid line represents in silico prediction, whereas dashed

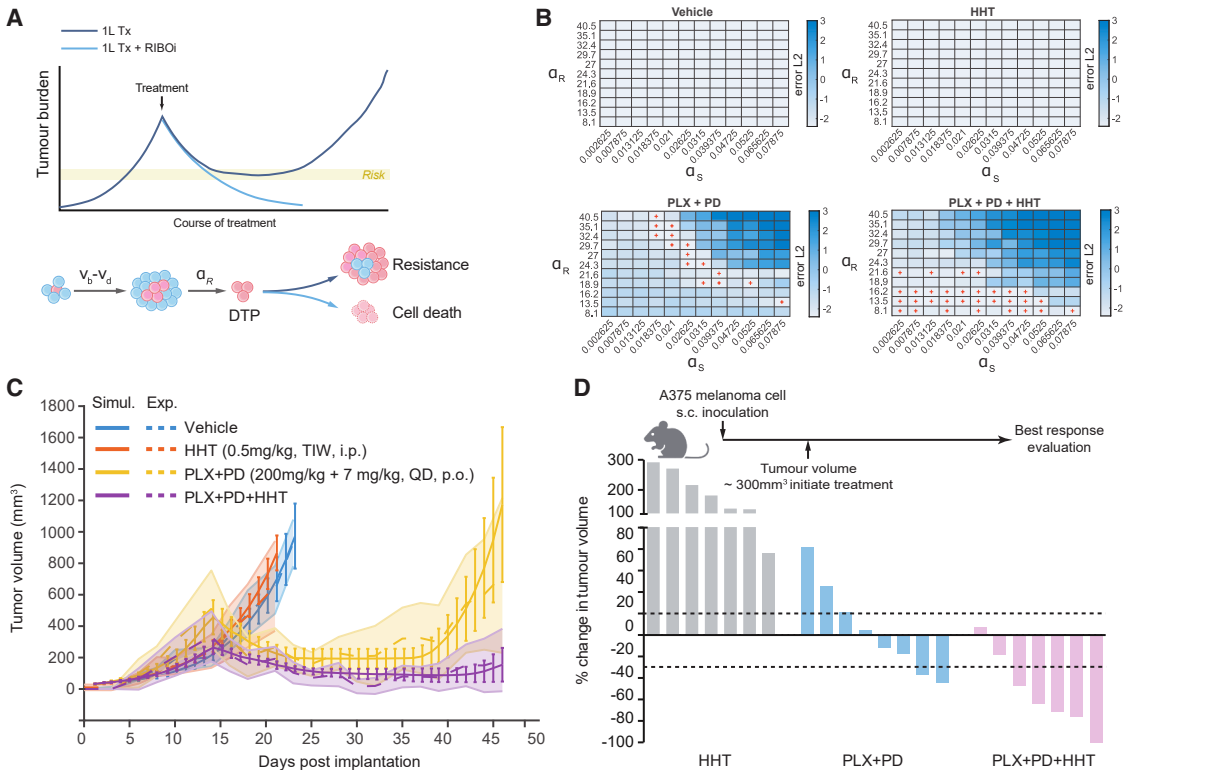

Figure 5. Targeting ribosome in combination with SOC treatment disrupts the "Risk" balance

(A) Schematic view of SOC treatment (Tx) in combination with ribosome inhibitor (RIBOi). v_b, proliferation rate of tumor cells; v_d, death rate of tumor cells.

(B) Parameter space impacting on the distance between experimental data and simulation results. By altering both ribosome adaptation speed α_R and the speed of resistance acquisition α_s, decrease of α_R can systematically better simulate the experimental results by fixing α_s. Red cross, represents the qualitative fitting between experimental data and simulation results.

See also Figure S8.

(C) Evolution of tumor volume of melanoma cells under different type of treatment regimens in nude mice harboring $BRAF^{V600E}$-mutated A375 melanoma xenografts. Dashed lines: data from *in vivo* experiments. Solid lines: simulated data from the model. $N = 8$ mice in each group were subjected to treatment. Data are represented by mean ± SD.

(D) Waterfall plot of the best response after 30 days treatment in nude mice harboring $BRAF^{V600E}$-mutated A375 melanoma xenografts. The percentage changes of tumor volumes were calculated based on the tumor volume at 30 days after the initiation of the treatment compared to the original tumor volume at day 1.

line represents *in vivo* experimental observations. These results suggest that HHT monotherapy has minimal impact on tumor growth due to high ribosome abundances (overloaded regimen). In contrast, an increased response rate was observed by inhibiting ribosomes with HHT in combination with BRAFi/MEKi compared to BRAFi/MEKi combo treatment, as represented by waterfall plot (Figure 5D).

While the combination of treatments targeting both treatment-sensitive cancer cells (i.e., BRAFi/MEKi-sensitive cells) and DTP cells (i.e., ribosome inhibition) holds promise for significantly improving survival outcomes, the use of combination regimens often entails a heightened risk of toxicities. As a result, adaptive therapy has emerged as an alternative for patients with advanced-stage cancers, leveraging mechanisms of acquired resistance to enable drug-sensitive populations to outcompete resistant clones in a drug-free environment.[45,46] Ideally, strategically employed intermittent treatment may allow residual DTP cells to re-enter a cellular state that is both proliferative and retains treatment sensitivity.[47] This approach has the potential to prolong the effectiveness of the treatment by delaying the emergence of acquired resistance without additional combination treatment (Figure 6A). To explore the efficacy of various intermittent treatment regimens, we utilized our mathematical framework, aiming to compare response outcomes *in silico*. We defined two key time periods: T1, representing the time under treatment, and T2, representing the time during drug withdrawal (Figure 6A). This enabled the calculation of two clinically relevant outcomes: (1) the change in tumor volume after initial treatment, referred to as Q1, and (2) the change in tumor volume after one cycle of intermittent treatment, referred to as Q2 (Figure 6A). More precisely, given an initialization time T_0, an initial treatment of duration T_1, a drug-free interval of duration T_2 and a 10-day rechallenge, the functions Q_1 and Q_2 are defined as follows:

$$Q_1 = \frac{N(t = T_0) - N(t = T_0+T_1)}{N(t = T_0)},$$

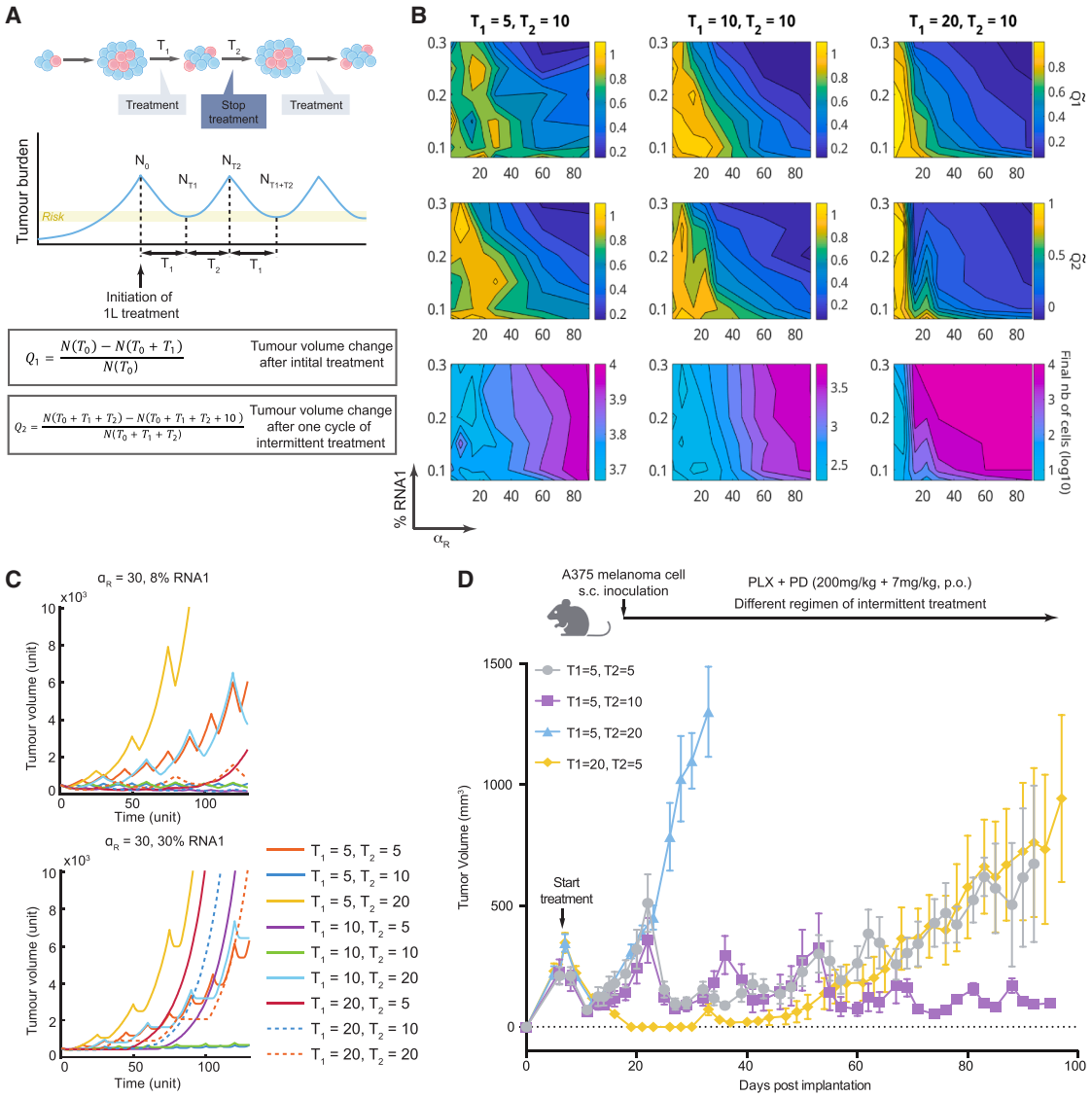

Figure 6. Intermittent treatment significantly slows down the rate of resistance acquisition

(A) Schematic view of intermittent treatment regimen. T_1, duration under treatment; T_2, duration of drug withdrawal; Q_1, tumor volume change after initial treatment; Q_2, tumor volume change after one cycle of intermittent treatment; N, tumor burden.

(B) Parameter space of initial percentage of RNA1 and ribosome adaptation speed α_R. Here, we show the resulting Q1 (top), Q2 (middle), final number of cells (log10) as a function of both initial %RNA1 and α_R.

See also Figure S9.

(C) *In silico* evolution of tumor burden under various intermittent treatment strategies. We start with N0 = 500 cells and alter the drug induction (T1) and drug holiday (T2) to simulate the tumor volume changes during 150 days.

(D) Experimental data of different intermittent treatment regimens in nude mice harboring $BRAF^{V600E}$-mutated A375 melanoma xenografts. Data are presented as mean ± SD, *n* = 6 mice each group.

$$Q_2 = \frac{N(t = T_0+T_1+T_2) - N(t = T_0+T_1+T_2+10)}{N(t = T_0+T_1+T_2)}.$$

Here, *N* (t = T) denotes the total number of cells at time T. These quantifiers are nondimensionalized by the reference values $\overline{Q}_1$ and $\overline{Q}_2$, computed as upper bounds of Q_1 and Q_2 under the assumption that all remain sensitive throughout the drug challenges. Under this assumption, the population declines exponentially at rate $\nu_b^* - \nu_0 < 0$ during treatment, yielding $N(t = T_0 + T_1) = N(t = T_0)e^{(\nu_b^* - \nu_0)T_1}$, and $N(t = T_0 + T_1 + T_2 + 10) = N(t = T_0 + T_1 + T_2)e^{(\nu_b^* - \nu_0)10}$, thus we got $\overline{Q}_1$ and $\overline{Q}_2$ as follows:

$$\overline{Q}_1 = 1 - e^{(\nu_b^* - \nu_0)T_1} = 1 - e^{-\nu_b^* T_1}$$

$$\overline{Q}_2 = 1 - e^{(\nu_b^* - \nu_0)10} = 1 - e^{-10\nu_b^*}.$$

Here, the second equalities follow from choosing $\nu_0 = 2\,\nu_b^*$. Using this expression for $\tilde{Q}_i = \frac{Q_i}{\overline{Q}_i}$, $\tilde{Q}_i$ thus equals 1 if all cells remain sensitive during re-challenge i, lies between 0 and 1 when a fraction of cells persists, and becomes negative when the population exhibits resistance. As shown in Figure 6B, we found that increasing ribosomal adaptation speed α_R favors the acquisition of persistence. However, this requires a minimal amount of RNA1 to be translated given that populations composed of less than 5% of RNA1 will never enter persister cell state (Figures 6B, S9A, and S9B). Our *in silico* analysis further underscores the impact of intermittent treatment duration on persistence and subsequent acquired resistance. Prolonging the treatment interval T1 result in more persistent populations (Figure 6B, right image compared to left image), which in turn accelerates the emergence of acquired resistance ($\tilde{Q} < 0$) when treatment durations are sufficiently long and release intervals sufficiently short.

To optimize intermittent treatment strategies without intervening ribosome adaptation by triple combination treatment as shown in Figure 5, we employed our mathematical model to consider intermittent treatments by varying T1 followed by drug holidays of varying T2 (Figures 6C and S9C). For systems with faster ribosome adaptation capacity (small α_R), both short T1 and T2 durations are conducive to better tumor volume control (Figure 6B). However, since we did not observe small $\alpha_R$based on our *in vivo* mouse experiment (Figure 5), this scenario does not align with our *in vivo* working model (A375 melanoma cells). It becomes evident that by fixing ribosomal adaptation speed $\alpha_R = 30$, shorter treatment durations T1 followed by longer drug-free intervals T2 (T2 > T1) lead to superior tumor volume control (Figure 6C). Nevertheless, excessively prolonged T2 durations may lead to uncontrolled cell proliferation and increase overall cell population, even in the absence of persistence (Figure 6B). Therefore, these *in silico* results underscore the necessity of tailoring the optimal intermittent treatment strategy based on ribosome adaptation speed α_R, which may vary depending on the cancer type and treatment regimen.

We further conducted *in vivo* experiment using A375 melanoma cells, which exhibited a ribosomal adaptation speed $\alpha_R = 30$ and resistance adaptation speed $\alpha_S = 0.0262$(Figure 5), and compared four different intermittent treatment regimens as simulated *in silico*. As shown in Figure 6D, a short treatment duration (T1 = 5 days) followed by a very long drug holiday (T2 = 20 days) led to rapid tumor growth (Figure 6D, blue line). Despite the potential sensitivity of these tumors to BRAFi/MEKi treatment, the rapid and uncontrollable tumor expansion renders this regimen impractical. Treatment regimens with extended treatment periods (T1 = 20 days) followed by brief drug holiday (T2 = 5 days), or short T1/T2 durations of 5 days each, demonstrated optimal control of tumor volume for approximately 60 days. However, tumor began exhibiting acquire resistance phenotypes and resumed growth after 60 days in both treatment regimens (Figure 6D, gray and yellow lines). This closely mirrors the outcomes observed with continuous treatment, as depicted in Figure 5, highlighting that both strategies fail to provide sufficient time for DTP cells to repopulate sensitive populations. Consistent with the *in silico* analysis, a short treatment duration (T1) of 5 days followed by an intermediate drug holiday (T2 = 10 days) showed promising tumor volume control (Figure 6D, purple line).

Intermittent drug treatment as a strategy to delay or prevent resistance has been explored across multiple cancer types and remains of interest for clinical investigation. This approach is motivated by the concept that resistance may incur evolutionary trade-offs, such that intermittent therapy could maintain competition between drug-sensitive and resistant cells and thereby slow the expansion of resistant populations. This principle has been demonstrated in preclinical ovarian cancer models, where adaptive carboplatin dosing based on tumor response prolonged survival compared with standard dosing without increasing overall drug exposure or toxicity.[48] However, translating these findings to the clinic remains challenging, largely because optimal drug-on and drug-off intervals are difficult to determine in patients. Notably, a phase 2 trial comparing continuous versus intermittent BRAFi/MEKi therapy in metastatic melanoma (NCT02196181) did not show a benefit of intermittent treatment using a fixed 3-week-off, 5-week-on schedule.[49] Together, these studies highlight the need for mechanistically informed strategies to guide intermittent treatment design. Our work provides a proof-of-concept framework that integrates ribosome competition principles to simulate and evaluate candidate intermittent treatment regimens in silico, thereby informing the design of subsequent *in vivo* studies and motivating further investigation into their potential translational relevance.

DISCUSSION

Ribosome biogenesis accounts for up to half of all newly synthesized proteins in eukaryotic cells.[50] This huge investment of resources results in the production of more than 1×10^5 RPs per minute in proliferative cells, requiring the synthesis, processing, and assembly of RPs and rRNAs in a coordinated fashion.[51] The small 40S ribosomal subunit contains one 18S rRNA and approximately 32 ribosomal proteins (RPS proteins) and the large 60S ribosomal subunit is composed of one of each 5S, 5.8S, and 28S rRNA, as well as approximately 47 ribosomal proteins (RPL proteins). Mature 40S and 60S subunits are then exported into the cytoplasm, where they assemble with mRNA to form the active translating 80S ribosome. Transcription of rRNA and mRNA encoding RPs is rapidly repressed upon nutrient limitation or environmental insults such as heat shock observed in eukaryotic cells, leading to reduced production of ribosomes. Reduced production of ribosomes limits cell proliferation,[52] providing a general mechanism for cells to slow growth during stress and liberate resources for processes essential to cell survival.

Our work revealed an additional regulatory layer beyond transcriptional and post-translational control mechanisms in cancer persistence. Specifically, we have identified a key factor in translational regulation: the limited access of mRNAs to ribosomes.[53] Within our mathematical framework, different mRNAs compete for the limited ribosome resources, particularly under drug insults. Higher-affinity transcripts have the capacity to displace lower-affinity ones from ribosomes, thereby enhancing their

own selective translational activity. This effect may be partially responsible for the poor correlation between transcript and protein levels.[54] While our findings suggest that reduced ribosome concentration can create a bottleneck effect in mRNA translation, we cannot exclude the possibility of selective translation due to specialized ribosomes, as indicated by our TMT mass spectrometry analysis of DTP cells. Indeed, the debate on translational dysfunction encompasses both the specialized ribosome hypothesis and the ribosome concentration hypothesis. The former posits that certain structural heterogeneities in ribosomes can stimulate the translation of specific mRNAs, as evidenced in studies such as those involving mice harboring mutated copies of eL38, which is specifically required for the translation of *Hox* mRNAs and loss of which lead to the animals with reduced body size, delayed development, and impaired fetal erythropoiesis.[55] A recent study in melanoma has also shown that a lncRNA-regulated specialized ribosomes may be involved in the melanoma tolerance to anti-PD1 immunotherapy.[56] On the contrary, reduced RP expression can disrupt ribosome assembly and decrease ribosome levels, a phenomenon investigated in ribosomopathies. RP haploinsufficiency, for example, is associated with DBA, while engineered increases in GATA1 protein levels can overcome the effects of heterozygous RP insufficiency in DBA patient cells.[57] Although earlier studies were not performed explicitly in the context of DTPs, they are highly relevant to understanding cancer persistence. DTPs are now recognized as a reservoir state that provides a temporal window for cells to accumulate mutations and ultimately give rise to stably resistant clones.[58,59] Pioneering work has shown that AXL mediated error-prone transcription or APOBEC-associated aberrant DNA deamination can contribute to this evolutionary transition in non-small cell lung cancer; however, these mechanisms primarily operate at the transcriptional level. Whether ribosomal selectivity itself participates in shaping the mutational landscape of DTPs remains an open and important question. Our previous work in melanoma persister cells uncovered a selective translation program in which ribosomes preferentially upregulate a subset of epigenetic regulators, including CBP and HDAC6, despite a global suppression of proliferation-associated translation.[7] Notably, DNA damage-response factors such as 53BP1 were also selectively translated.[7] This is particularly intriguing because 53BP1 promotes error-prone non-homologous end joining (NHEJ), raising the possibility that ribosome-mediated translational bias may directly modulate the mutability of DTPs. A recent study building on our findings demonstrated, using *in situ* proximity ligation assays, that ribosomes in melanoma persister cells physically engage the 53BP1 mRNA. Moreover, mutating the 5′UTR of 53BP1 to disrupt its cap-dependent translation was sufficient to attenuate DTP-associated NHEJ activity and reduce mutability.[60] Together, these studies suggest that selective translation is not merely a passive response to therapy stress but may actively sculpt the evolution of DTPs toward acquired resistance—an area warranting deeper mechanistic investigation.

To our knowledge, ribosome-selection mechanisms have not yet been incorporated into modeling frameworks aimed at understanding DTP dynamics or informing treatment strategies. Our work introduces this dimension by demonstrating, from a mathematical perspective, that quantitative shifts in ribosome availability can themselves generate selective translational outcomes. This emerges from the inherently nonlinear relationship between translation-initiation rates and the concentration of available ribosomes. In this context, the relationship can be expressed as the effective protein synthesis of individual mRNA being proportional to the product m*R*k_i, where m represents the expression level of corresponding mRNA, R stands for the ribosome concentration and k_i represents the mRNA-specific translation rate constant.[61] Additionally, factors such as mRNA length and the number of ribosomes on corresponding transcripts contribute to selective translational regulation. This relationship between protein synthesis rate and available ribosome concentrations is encapsulated in the following equation $Q = mRk_i\left[1 - \frac{L}{\frac{k_e}{k_i R^{+(L-1)}}}\right]$, where Q represents the protein synthesis rate, k_e is the termination rate, and L is the density of ribosome over the transcripts.[62] This insight underscores that a transcript with high affinity or initiation rate is effectively translated even at lower concentrations of ribosomes,[63] which was integrated as a regulatory parameter (τ_i) in our model. However, whether τ_i is directly controlled by m6A modification in the transcripts requires further experimental validation, potentially through *in vitro* translation assays.[64] In light of the intrinsic mutability of DTPs, our mathematical framework could be extended to incorporate the mutational trajectories that shape the later phases of acquired resistance. In the current model, resistance is simplified as a progressive reduction in drug-induced death rates under continuous treatment; once cellular sensitivity falls below a defined threshold, cells transition into an irreversible resistant state. At that point, they reinitiate ribosome biogenesis to restore proliferative capacity despite ongoing drug exposure. Future iterations of the model should integrate DNA damage-associated regulators—such as 53BP1—as proxies for translationally controlled mutability.[60] Embedding such factors into the translation-competition framework would allow the model to capture how selective translation programs may actively steer the evolutionary path from drug tolerance to fixed resistance. Achieving this integration will require next-generation technologies capable of resolving selective translation with sufficient temporal and molecular precision in DTPs.[65] Such high-resolution measurements will be essential for accurately parameterizing a more complete mathematical model and for capturing how dynamic translational rewiring contributes to the evolutionary trajectories of drug tolerance and resistance.

Limitations of the study

Although our current framework delineates the importance of a ribosomal threshold for DTP survival under therapeutic pressure—and the model can estimate optimal timing for combination treatments—several limitations remain and warrant further investigation. We identified c-Myc, a master regulator of ribosome biogenesis, as a contributor to the ribosome bottleneck observed in DTPs. However, additional mechanisms may also participate. For example, the integrated stress response (ISR) has been implicated as a key driver of translational adaptation

to both chemotherapy and targeted therapy.[66] By integrating diverse stress cues, the ISR suppresses global cap-dependent translation while enabling ATF4-mediated transcriptional and translational remodeling, ultimately supporting DTP survival.[67] Future work should incorporate such regulatory pathways into our mathematical framework to more fully capture the determinants of selective translation. A second limitation arises from the relevance between *in vitro* and *in vivo* observations. While polysome profiling revealed global translational downregulation in cell line models, this pattern has not yet been explored *in vivo*, particularly in the context of minimal residual disease. Profiling translation in residual tumor cells *in vivo* remains technically challenging due to unavoidable admixture of tumor and stromal compartments. Thus, emerging technologies—such as single-cell ribosome sequencing[68] and spatially resolved single-cell translatomics[69]—should be adapted to residual-disease settings to enable high-resolution dissection of translational regulation *in vivo*. Furthermore, our current framework does not yet incorporate microenvironmental factors that shape DTP behavior, underscoring the need for experimental data generated in immunocompetent models. This is particularly important because competition for nutrients between tumor and stromal cells can substantially remodel the translational landscape. The degree to which immune pressure further fine-tunes tumor-cell translation remains largely unknown. Environmental cues such as nutrient availability can profoundly modulate translation; for example, amino acid scarcity regulates wobble-uridine (U34) modification in specific tRNAs,[70] via ELP1/ELP3, thereby altering Hypoxia-inducible factor-1 alpha (HIF1α) translation and metabolic adaptation in melanoma cells.[71] These examples highlight only a small fraction of the microenvironmental influences likely at play in DTPs.

Looking forward, both experimental and mathematical investigations should move toward more systemic and clinically relevant settings by integrating microenvironmental inputs, immune-cell interactions, and host-level variables such as metabolic status and aging.[65] As single-cell technologies and longitudinal sampling advance in preclinical and clinical models, our simplified framework could be expanded through agent-based modeling to capture cell-cell interactions, as well as spatial modeling to incorporate drug diffusion and cytokine gradients. These developments will be essential for translating mathematical predictions into clinically actionable strategies. Despite its current limitations, our framework provides a foundational platform for incorporating diverse regulatory layers contributing to cancer persistence and offers a systematic approach for exploring therapeutic interventions. More broadly, it underscores a ribosome-controlled mechanism through which DTPs may strategically assume "risk" to enhance their long-term survival.

RESOURCE AVAILABILITY

Lead contact

Further data of this study, the related reagents, and technical protocols should be contacted to the lead contact, Shensi Shen (shensi.sean@gmail.com).

Materials availability

This study did not generate new unique reagents.

Data and code availability

- RNA-seq data have been deposited at Gene Expression Omnibus (GEO) as GEO: GSE313946 and are publicly available as of the date of publication. The mass spectrometry proteomics data have been deposited to ProteomeXchange (https://proteomecentral.proteomexchange.org) as ProteomeXchange: PXD052572.
- This study does not report original code.
- Any additional information required to reanalyze the data reported in this paper is available from the lead contact upon request.

ACKNOWLEDGMENTS

S.S. acknowledges grant support from National Natural Science Foundation of China (grant nos. 82172794 and 82473387), National Clinical Research Center for Geriatrics, West China Hospital ofSichuan University (grant no. Y2022JC002). D.P. was supported by Agence Nationale de la Recherche (ANR) under the project grant no. ANR-22-CE45-0024-01. X.T. was supported by the postdoctoral fellowship program of CPSF (grant no. GZC20241146) and the Sichuan Science and Technology Program (grant no. 2025ZNSFSC1860). C.R. thanks S. Bazin, O. and C. Courtin, Ensemble Contre le Mélanome, the Foundation Crédit Mutuel, Foundation Carrefour and the association Vaincre le Mélanome for their ongoing research funding support.

AUTHOR CONTRIBUTIONS

X.T., Y.W., and Y.P. performed *in vitro* and *in vivo* experiments; K.L., M.W., M.C., Y.C. performed *in vivo* experiments; Z.D. and M.C. performed polysome RNAseq and analyses; L.A. and D.P. constructed the mathematical models and numerical analyses; D.P., C.R., and S.S. performed data analyses, supervised the study, and wrote the manuscript.

DECLARATION OF INTERESTS

C.R. has acted as a consultant for Astra Zeneca, BMS, MSD, Pfizer, Pierre Fabre, Roche and Sanofi and is a co-founder of Ribonexus. M.C. is a CSO for BiPer Therapeutics (Strasbourg, France). S.S. reports personal fees from Agence nationale de la recherche (France), Krebsliga Schweiz (Switzerland), KWF Kankerbestrijding (the Netherlands), Institut national de la santé et de la recherche médicale (France), and Shenzhen Medical Academy of Research and Translation (China).

STAR★METHODS

Detailed methods are provided in the online version of this paper and include the following:

- KEY RESOURCES TABLE
- EXPERIMENTAL MODEL AND STUDY PARTICIPANT DETAILS
  - Experimental animals
  - Cell lines
  - Human subjects
  - Reagents
  - Production of drug-tolerant persister cells
- METHOD DETAILS
  - Polysome profiling measuring translational activity
  - Clonogenic assay
  - Western blotting analysis
  - Lentiviral shRNA stable cell lines
  - RNA isolation and quantitative RT-PCR
  - Mouse xenograft experiments
  - Immunofluorescence microscopy
  - Image-based supervised classification using CellProfiler
  - TMT based quantitative mass spectrometry
  - Harringtonine run-off assays
  - Chromatin immunoprecipitation (ChIP)-quantitative PCR
  - Polysome RNA extraction
  - Polysome RNA library preparation for transcriptome sequencing

- Polysome RNA bioinformatics analysis - Xtail
- QUANTIFICATION AND STATISTICAL ANALYSIS

SUPPLEMENTAL INFORMATION

Supplemental information can be found online at https://doi.org/10.1016/j.isci.2026.115493.

Received: June 17, 2025
Revised: December 17, 2025
Accepted: March 24, 2026
Published: March 27, 2026

REFERENCES

1. Sharma, P., Hu-Lieskovan, S., Wargo, J.A., and Ribas, A. (2017). Primary, Adaptive, and Acquired Resistance to Cancer Immunotherapy. Cell *168*, 707–723. https://doi.org/10.1016/j.cell.2017.01.017.
2. Marine, J.C., Dawson, S.J., and Dawson, M.A. (2020). Non-genetic mechanisms of therapeutic resistance in cancer. Nat. Rev. Cancer *20*, 743–756. https://doi.org/10.1038/s41568-020-00302-4.
3. Marin-Bejar, O., Rogiers, A., Dewaele, M., Femel, J., Karras, P., Pozniak, J., Bervoets, G., Van Raemdonck, N., Pedri, D., Swings, T., et al. (2021). Evolutionary predictability of genetic versus nongenetic resistance to anticancer drugs in melanoma. Cancer Cell *39*, 1135–1149.e8. https://doi.org/10.1016/j.ccell.2021.05.015.
4. Sharma, S.V., Lee, D.Y., Li, B., Quinlan, M.P., Takahashi, F., Maheswaran, S., McDermott, U., Azizian, N., Zou, L., Fischbach, M.A., et al. (2010). A chromatin-mediated reversible drug-tolerant state in cancer cell subpopulations. Cell *141*, 69–80. https://doi.org/10.1016/j.cell.2010.02.027.
5. Shen, S., Vagner, S., and Robert, C. (2020). Persistent Cancer Cells: The Deadly Survivors. Cell *183*, 860–874. https://doi.org/10.1016/j.cell.2020.10.027.
6. Pu, Y., Li, L., Peng, H., Liu, L., Heymann, D., Robert, C., Vallette, F., and Shen, S. (2023). Drug-tolerant persister cells in cancer: the cutting edges and future directions. Nat. Rev. Clin. Oncol. *20*, 799–813. https://doi.org/10.1038/s41571-023-00815-5.
7. Shen, S., Faouzi, S., Bastide, A., Martineau, S., Malka-Mahieu, H., Fu, Y., Sun, X., Mateus, C., Routier, E., Roy, S., et al. (2019). An epitranscriptomic mechanism underlies selective mRNA translation remodelling in melanoma persister cells. Nat. Commun. *10*, 5713. https://doi.org/10.1038/s41467-019-13360-6.
8. Shen, S., and Sun, X. (2020). Emerging role of mRNA epitranscriptomic regulation in chemoresistant cancer cells. Mol. Cell. Oncol. *7*, 1728467. https://doi.org/10.1080/23723556.2020.1728467.
9. Genuth, N.R., and Barna, M. (2018). The Discovery of Ribosome Heterogeneity and Its Implications for Gene Regulation and Organismal Life. Mol. Cell *71*, 364–374. https://doi.org/10.1016/j.molcel.2018.07.018.
10. Xue, S., Tian, S., Fujii, K., Kladwang, W., Das, R., and Barna, M. (2015). RNA regulons in Hox 5' UTRs confer ribosome specificity to gene regulation. Nature *517*, 33–38. https://doi.org/10.1038/nature14010.
11. Guimaraes, J.C., and Zavolan, M. (2016). Patterns of ribosomal protein expression specify normal and malignant human cells. Genome Biol. *17*, 236. https://doi.org/10.1186/s13059-016-1104-z.
12. Khajuria, R.K., Munschauer, M., Ulirsch, J.C., Fiorini, C., Ludwig, L.S., McFarland, S.K., Abdulhay, N.J., Specht, H., Keshishian, H., Mani, D.R., et al. (2018). Ribosome Levels Selectively Regulate Translation and Lineage Commitment in Human Hematopoiesis. Cell *173*, 90–103.e19. https://doi.org/10.1016/j.cell.2018.02.036.
13. Kovalski, J.R., Kuzuoglu-Ozturk, D., and Ruggero, D. (2022). Protein synthesis control in cancer: selectivity and therapeutic targeting. EMBO J. *41*, e109823. https://doi.org/10.15252/embj.2021109823.
14. Klumpp, S., and Hwa, T. (2008). Growth-rate-dependent partitioning of RNA polymerases in bacteria. Proc. Natl. Acad. Sci. USA *105*, 20245–20250. https://doi.org/10.1073/pnas.0804953105.
15. Mauro, V.P., and Edelman, G.M. (2002). The ribosome filter hypothesis. Proc. Natl. Acad. Sci. USA *99*, 12031–12036. https://doi.org/10.1073/pnas.192442499.
16. Scott, M., Gunderson, C.W., Mateescu, E.M., Zhang, Z., and Hwa, T. (2010). Interdependence of cell growth and gene expression: origins and consequences. Science *330*, 1099–1102. https://doi.org/10.1126/science.1192588.
17. Baumgartner, B.L., Bennett, M.R., Ferry, M., Johnson, T.L., Tsimring, L.S., and Hasty, J. (2011). Antagonistic gene transcripts regulate adaptation to new growth environments. Proc. Natl. Acad. Sci. USA *108*, 21087–21092. https://doi.org/10.1073/pnas.1111408109.
18. Gillies, R.J., Brown, J.S., Anderson, A.R.A., and Gatenby, R.A. (2018). Eco-evolutionary causes and consequences of temporal changes in intratumoural blood flow. Nat. Rev. Cancer *18*, 576–585. https://doi.org/10.1038/s41568-018-0030-7.
19. Altrock, P.M., Liu, L.L., and Michor, F. (2015). The mathematics of cancer: integrating quantitative models. Nat. Rev. Cancer *15*, 730–745. https://doi.org/10.1038/nrc4029.
20. Russo, M., Pompei, S., Sogari, A., Corigliano, M., Crisafulli, G., Puliafito, A., Lamba, S., Erriquez, J., Bertotti, A., Gherardi, M., et al. (2022). A modified fluctuation-test framework characterizes the population dynamics and mutation rate of colorectal cancer persister cells. Nat. Genet. *54*, 976–984. https://doi.org/10.1038/s41588-022-01105-z.
21. Chisholm, R.H., Lorenzi, T., Lorz, A., Larsen, A.K., de Almeida, L.N., Escargueil, A., and Clairambault, J. (2015). Emergence of drug tolerance in cancer cell populations: an evolutionary outcome of selection, nongenetic instability, and stress-induced adaptation. Cancer Res. *75*, 930–939. https://doi.org/10.1158/0008-5472.CAN-14-2103.
22. Song, C., Piva, M., Sun, L., Hong, A., Moriceau, G., Kong, X., Zhang, H., Lomeli, S., Qian, J., Yu, C.C., et al. (2017). Recurrent Tumor Cell-Intrinsic and -Extrinsic Alterations during MAPKi-Induced Melanoma Regression and Early Adaptation. Cancer Discov. *7*, 1248–1265. https://doi.org/10.1158/2159-8290.CD-17-0401.
23. Hugo, W., Shi, H., Sun, L., Piva, M., Song, C., Kong, X., Moriceau, G., Hong, A., Dahlman, K.B., Johnson, D.B., et al. (2015). Non-genomic and Immune Evolution of Melanoma Acquiring MAPKi Resistance. Cell *162*, 1271–1285. https://doi.org/10.1016/j.cell.2015.07.061.
24. van Riggelen, J., Yetil, A., and Felsher, D.W. (2010). MYC as a regulator of ribosome biogenesis and protein synthesis. Nat. Rev. Cancer *10*, 301–309. https://doi.org/10.1038/nrc2819.
25. Simsek, D., Tiu, G.C., Flynn, R.A., Byeon, G.W., Leppek, K., Xu, A.F., Chang, H.Y., and Barna, M. (2017). The Mammalian Ribo-interactome Reveals Ribosome Functional Diversity and Heterogeneity. Cell *169*, 1051–1065.e18. https://doi.org/10.1016/j.cell.2017.05.022.
26. Thompson, A., Schäfer, J., Kuhn, K., Kienle, S., Schwarz, J., Schmidt, G., Neumann, T., Johnstone, R., Mohammed, A.K.A., and Hamon, C. (2003). Tandem mass tags: a novel quantification strategy for comparative analysis of complex protein mixtures by MS/MS. Anal. Chem. *75*, 1895–1904. https://doi.org/10.1021/ac0262560.
27. Genuth, N.R., Shi, Z., Kunimoto, K., Hung, V., Xu, A.F., Kerr, C.H., Tiu, G.C., Oses-Prieto, J.A., Salomon-Shulman, R.E.A., Axelrod, J.D., et al. (2022). A stem cell roadmap of ribosome heterogeneity reveals a function for RPL10A in mesoderm production. Nat. Commun. *13*, 5491. https://doi.org/10.1038/s41467-022-33263-3.
28. Tsherniak, A., Vazquez, F., Montgomery, P.G., Weir, B.A., Kryukov, G., Cowley, G.S., Gill, S., Harrington, W.F., Pantel, S., Krill-Burger, J.M., et al. (2017). Defining a Cancer Dependency Map. Cell *170*, 564–576.e16. https://doi.org/10.1016/j.cell.2017.06.010.

29. Yan, L.L., and Zaher, H.S. (2021). Ribosome quality control antagonizes the activation of the integrated stress response on colliding ribosomes. Mol. Cell *81*, 614–628.e4. https://doi.org/10.1016/j.molcel.2020.11.033.

30. Ingolia, N.T., Lareau, L.F., and Weissman, J.S. (2011). Ribosome profiling of mouse embryonic stem cells reveals the complexity and dynamics of mammalian proteomes. Cell *147*, 789–802. https://doi.org/10.1016/j.cell.2011.10.002.

31. Conn, C.S., and Qian, S.B. (2013). Nutrient signaling in protein homeostasis: an increase in quantity at the expense of quality. Sci. Signal. *6*, ra24. https://doi.org/10.1126/scisignal.2003520.

32. Geuens, T., Bouhy, D., and Timmerman, V. (2016). The hnRNP family: insights into their role in health and disease. Hum. Genet. *135*, 851–867. https://doi.org/10.1007/s00439-016-1683-5.

33. Shen, S., Faouzi, S., Souquere, S., Roy, S., Routier, E., Libenciuc, C., André, F., Pierron, G., Scoazec, J.Y., and Robert, C. (2020). Melanoma Persister Cells Are Tolerant to BRAF/MEK Inhibitors via ACOX1-Mediated Fatty Acid Oxidation. Cell Rep. *33*, 108421. https://doi.org/10.1016/j.celrep.2020.108421.

34. Carpenter, A.E., Jones, T.R., Lamprecht, M.R., Clarke, C., Kang, I.H., Friman, O., Guertin, D.A., Chang, J.H., Lindquist, R.A., Moffat, J., et al. (2006). CellProfiler: image analysis software for identifying and quantifying cell phenotypes. Genome Biol. *7*, R100. https://doi.org/10.1186/gb-2006-7-10-r100.

35. Abraham, K.J., Khosraviani, N., Chan, J.N.Y., Gorthi, A., Samman, A., Zhao, D.Y., Wang, M., Bokros, M., Vidya, E., Ostrowski, L.A., et al. (2020). Nucleolar RNA polymerase II drives ribosome biogenesis. Nature *585*, 298–302. https://doi.org/10.1038/s41586-020-2497-0.

36. Grandori, C., Gomez-Roman, N., Felton-Edkins, Z.A., Ngouenet, C., Galloway, D.A., Eisenman, R.N., and White, R.J. (2005). c-Myc binds to human ribosomal DNA and stimulates transcription of rRNA genes by RNA polymerase I. Nat. Cell Biol. *7*, 311–318. https://doi.org/10.1038/ncb1224.

37. Asmussen, S. (2003). Applied Probability and Queues (Springer-Verlag).

38. Cookson, N.A., Mather, W.H., Danino, T., Mondragón-Palomino, O., Williams, R.J., Tsimring, L.S., and Hasty, J. (2011). Queueing up for enzymatic processing: correlated signaling through coupled degradation. Mol. Syst. Biol. *7*, 561. https://doi.org/10.1038/msb.2011.94.

39. Vaghi, C., Rodallec, A., Fanciullino, R., Ciccolini, J., Mochel, J.P., Mastri, M., Poignard, C., Ebos, J.M.L., and Benzekry, S. (2020). Population modeling of tumor growth curves and the reduced Gompertz model improve prediction of the age of experimental tumors. PLoS Comput. Biol. *16*, e1007178. https://doi.org/10.1371/journal.pcbi.1007178.

40. Burger, K., Mühl, B., Harasim, T., Rohrmoser, M., Malamoussi, A., Orban, M., Kellner, M., Gruber-Eber, A., Kremmer, E., Hölzel, M., and Eick, D. (2010). Chemotherapeutic drugs inhibit ribosome biogenesis at various levels. J. Biol. Chem. *285*, 12416–12425. https://doi.org/10.1074/jbc.M109.074211.

41. Tye, B.W., Commins, N., Ryazanova, L.V., Wühr, M., Springer, M., Pincus, D., and Churchman, L.S. (2019). Proteotoxicity from aberrant ribosome biogenesis compromises cell fitness. eLife *8*, e43002. https://doi.org/10.7554/eLife.43002.

42. Ni, C., Wei, Y., Vona, B., Park, D., Wei, Y., Schmitz, D.A., Ding, Y., Sakurai, M., Ballard, E., Li, L., et al. (2025). A programmed decline in ribosome levels governs human early neurodevelopment. Nat. Cell Biol. *27*, 1240–1255. https://doi.org/10.1038/s41556-025-01708-8.

43. Garreau de Loubresse, N., Prokhorova, I., Holtkamp, W., Rodnina, M.V., Yusupova, G., and Yusupov, M. (2014). Structural basis for the inhibition of the eukaryotic ribosome. Nature *513*, 517–522. https://doi.org/10.1038/nature13737.

44. Kantarjian, H.M., Talpaz, M., Santini, V., Murgo, A., Cheson, B., and O'Brien, S.M. (2001). Homoharringtonine: history, current research, and future direction. Cancer *92*, 1591–1605. https://doi.org/10.1002/1097-0142(20010915)92:6<1591::aid-cncr1485>3.0.co;2-u.

45. Enriquez-Navas, P.M., Kam, Y., Das, T., Hassan, S., Silva, A., Foroutan, P., Ruiz, E., Martinez, G., Minton, S., Gillies, R.J., and Gatenby, R.A. (2016). Exploiting evolutionary principles to prolong tumor control in preclinical models of breast cancer. Sci. Transl. Med. *8*, 327ra24. https://doi.org/10.1126/scitranslmed.aad7842.

46. Labrie, M., Brugge, J.S., Mills, G.B., and Zervantonakis, I.K. (2022). Therapy resistance: opportunities created by adaptive responses to targeted therapies in cancer. Nat. Rev. Cancer *22*, 323–339. https://doi.org/10.1038/s41568-022-00454-5.

47. Kuczynski, E.A., Sargent, D.J., Grothey, A., and Kerbel, R.S. (2013). Drug rechallenge and treatment beyond progression–implications for drug resistance. Nat. Rev. Clin. Oncol. *10*, 571–587. https://doi.org/10.1038/nrclinonc.2013.158.

48. Hockings, H., Lakatos, E., Huang, W., Mossner, M., Khan, M.A., Bakali, N., McDermott, J., Smith, K., Baker, A.M., Graham, T.A., and Lockley, M. (2025). Adaptive Therapy Exploits Fitness Deficits in Chemotherapy-Resistant Ovarian Cancer to Achieve Long-Term Tumor Control. Cancer Res. *85*, 3503–3517. https://doi.org/10.1158/0008-5472.CAN-25-0351.

49. Algazi, A.P., Othus, M., Daud, A.I., Lo, R.S., Mehnert, J.M., Truong, T.G., Conry, R., Kendra, K., Doolittle, G.C., Clark, J.I., et al. (2020). Continuous versus intermittent BRAF and MEK inhibition in patients with BRAF-mutated melanoma: a randomized phase 2 trial. Nat. Med. *26*, 1564–1568. https://doi.org/10.1038/s41591-020-1060-8.

50. Ingolia, N.T., Ghaemmaghami, S., Newman, J.R.S., and Weissman, J.S. (2009). Genome-wide analysis in vivo of translation with nucleotide resolution using ribosome profiling. Science *324*, 218–223. https://doi.org/10.1126/science.1168978.

51. Shore, D., and Albert, B. (2022). Ribosome biogenesis and the cellular energy economy. Curr. Biol. *32*, R611–R617. https://doi.org/10.1016/j.cub.2022.04.083.

52. Shore, D., Zencir, S., and Albert, B. (2021). Transcriptional control of ribosome biogenesis in yeast: links to growth and stress signals. Biochem. Soc. Trans. *49*, 1589–1599. https://doi.org/10.1042/BST20201136.

53. Gebauer, F., and Hentze, M.W. (2004). Molecular mechanisms of translational control. Nat. Rev. Mol. Cell Biol. *5*, 827–835. https://doi.org/10.1038/nrm1488.

54. Mills, E.W., and Green, R. (2017). Ribosomopathies: There's strength in numbers. Science *358*, eaan2755. https://doi.org/10.1126/science.aan2755.

55. Morgan, W.C. (1950). A new tail-short mutation in the mouse whose lethal effects are conditioned by the residual genotypes. J. Hered. *41*, 208–215. https://doi.org/10.1093/oxfordjournals.jhered.a106131.

56. Cinque, S., Verheyden, Y., Adnane, S., Marino, A., Hanache, S., Vendramin, R., Cuomo, A., Pozniak, J., Calabuig, A.C., Baldewijins, M., Tabruyn, S., et al. (2026). The assembly of cancer-specific ribosomes by the lncRNA LISRR suppresses melanoma anti-tumor immunity. J. Exp. Med. *223*, e20251507. https://doi.org/10.1084/jem.20251507.

57. Ludwig, L.S., Gazda, H.T., Eng, J.C., Eichhorn, S.W., Thiru, P., Ghazvinian, R., George, T.I., Gotlib, J.R., Beggs, A.H., Sieff, C.A., et al. (2014). Altered translation of GATA1 in Diamond-Blackfan anemia. Nat. Med. *20*, 748–753. https://doi.org/10.1038/nm.3557.

58. Noronha, A., Belugali Nataraj, N., Lee, J.S., Zhitomirsky, B., Oren, Y., Oster, S., Lindzen, M., Mukherjee, S., Will, R., Ghosh, S., et al. (2022). AXL and Error-Prone DNA Replication Confer Drug Resistance and Offer Strategies to Treat EGFR-Mutant Lung Cancer. Cancer Discov. *12*, 2666–2683. https://doi.org/10.1158/2159-8290.CD-22-0111.

59. Isozaki, H., Sakhtemani, R., Abbasi, A., Nikpour, N., Stanzione, M., Oh, S., Langenbucher, A., Monroe, S., Su, W., Cabanos, H.F., et al. (2023). Therapy-induced APOBEC3A drives evolution of persistent cancer cells. Nature *620*, 393–401. https://doi.org/10.1038/s41586-023-06303-1.

60. Fabbri, L., L., L., Guérin, E., Lecourt, H., Baille, D., Besse, L., Messaoudi, C., Désaubry, L., Abou-Hamdan, H., Roy, S., et al. (2025). Selective mRNA translation determines adaptative mutability of melanoma cells to

anti-BRAF/MEK combination therapy. Preprint at bioRxiv. https://doi.org/10.1101/2025.09.02.673634.

61. Lodish, H.F. (1974). Model for the regulation of mRNA translation applied to haemoglobin synthesis. Nature *251*, 385–388. https://doi.org/10.1038/251385a0.

62. Kim, M.S., Pinto, S.M., Getnet, D., Nirujogi, R.S., Manda, S.S., Chaerkady, R., Madugundu, A.K., Kelkar, D.S., Isserlin, R., Jain, S., et al. (2014). A draft map of the human proteome. Nature *509*, 575–581. https://doi.org/10.1038/nature13302.

63. Horos, R., Ijspeert, H., Pospisilova, D., Sendtner, R., Andrieu-Soler, C., Taskesen, E., Nieradka, A., Cmejla, R., Sendtner, M., Touw, I.P., and von Lindern, M. (2012). Ribosomal deficiencies in Diamond-Blackfan anemia impair translation of transcripts essential for differentiation of murine and human erythroblasts. Blood *119*, 262–272. https://doi.org/10.1182/blood-2011-06-358200.

64. Snieckute, G., Ryder, L., Vind, A.C., Wu, Z., Arendrup, F.S., Stoneley, M., Chamois, S., Martinez-Val, A., Leleu, M., Dreos, R., et al. (2023). ROS-induced ribosome impairment underlies ZAKalpha-mediated metabolic decline in obesity and aging. Science *382*, eadf3208. https://doi.org/10.1126/science.adf3208.

65. Wang, Z., Wang, M., Dong, B., Wang, Y., Ding, Z., and Shen, S. (2025). Drug-tolerant persister cells in cancer: bridging the gaps between bench and bedside. Nat. Commun. *16*, 10048. https://doi.org/10.1038/s41467-025-66376-6.

66. Falletta, P., Sanchez-Del-Campo, L., Chauhan, J., Effern, M., Kenyon, A., Kershaw, C.J., Siddaway, R., Lisle, R., Freter, R., Daniels, M.J., et al. (2017). Translation reprogramming is an evolutionarily conserved driver of phenotypic plasticity and therapeutic resistance in melanoma. Genes Dev. *31*, 18–33. https://doi.org/10.1101/gad.290940.116.

67. Vivas-García, Y., Falletta, P., Liebing, J., Louphrasitthiphol, P., Feng, Y., Chauhan, J., Scott, D.A., Glodde, N., Chocarro-Calvo, A., Bonham, S., et al. (2020). Lineage-Restricted Regulation of SCD and Fatty Acid Saturation by MITF Controls Melanoma Phenotypic Plasticity. Mol. Cell *77*, 120–137.e9. https://doi.org/10.1016/j.molcel.2019.10.014.

68. VanInsberghe, M., van den Berg, J., Andersson-Rolf, A., Clevers, H., and van Oudenaarden, A. (2021). Single-cell Ribo-seq reveals cell cycle-dependent translational pausing. Nature *597*, 561–565. https://doi.org/10.1038/s41586-021-03887-4.

69. Zeng, H., Huang, J., Ren, J., Wang, C.K., Tang, Z., Zhou, H., Zhou, Y., Shi, H., Aditham, A., Sui, X., et al. (2023). Spatially resolved single-cell translatomics at molecular resolution. Science *380*, eadd3067. https://doi.org/10.1126/science.add3067.

70. Laxman, S., Sutter, B.M., Wu, X., Kumar, S., Guo, X., Trudgian, D.C., Mirzaei, H., and Tu, B.P. (2013). Sulfur amino acids regulate translational capacity and metabolic homeostasis through modulation of tRNA thiolation. Cell *154*, 416–429. https://doi.org/10.1016/j.cell.2013.06.043.

71. Rapino, F., Delaunay, S., Rambow, F., Zhou, Z., Tharun, L., De Tullio, P., Sin, O., Shostak, K., Schmitz, S., Piepers, J., et al. (2018). Codon-specific translation reprogramming promotes resistance to targeted therapy. Nature *558*, 605–609. https://doi.org/10.1038/s41586-018-0243-7.

72. Knight, J.R.P., Bastide, A., Roobol, A., Roobol, J., Jackson, T.J., Utami, W., Barrett, D.A., Smales, C.M., and Willis, A.E. (2015). Eukaryotic elongation factor 2 kinase regulates the cold stress response by slowing translation elongation. Biochem. J. *465*, 227–238. https://doi.org/10.1042/BJ20141014.

STAR★METHODS

KEY RESOURCES TABLE

REAGENT or RESOURCE	SOURCE	IDENTIFIER
Antibodies		
cMyc	Cell Signaling Technology	Cat# 9402s, RRID: AB_2151827
RPL7	Proteintech	Cat# 14583-1-AP, RRID: AB_2254049
RPS15	Proteintech	Cat# 14957-1-AP, RRID: AB_2180163
RPS6	Cell Signaling Technology	Cat# 2217, RRID: AB_331355
Anti-Ki67	Proteintech	Cat# 27309-1-AP, RRID:AB_2756525
Anti-PES1	Abcam	Cat# ab88543, RRID:AB_2299416
Anti-NPM1	DSHB	Cat#PCRP-NPM1-1B4, RRID:AB_2722277
HRP-conjugated secondary antibodies	Sigma-Aldrich	Cat# 12-348, RRID:AB_390191
Chemicals, peptides, and recombinant proteins		
Vemurafenib	Selleck	Cat# S1267
Cobimetinib	Selleck	Cat# S8041
Homoharringtonine (CGX-635)	Selleck	Cat# S9015
Harringtonine	Selleck	Cat# S9063
Gemcitabine	Selleck	Cat# S1714
Cisplatin	Selleck	Cat# S1166
Cycloheximide (CHX)	Sigma-Aldrich	Cat# C104450
PLX-4720 (BRAFi)	Lebomei (China)	Cat# 918505-84-7
PD0325901 (MEKi)	Lebomei (China)	Cat# 391210-10-9
DMEM growth media	Gibco	Cat#C11995500BT
Glutamine	Gibco	Cat#A2916801
RPMI1640	Gibco	Cat#C11875500BT
Triton X-100	Merck	Cat#9036-19-5
Sodium deoxycholate	Merck	Cat#302-95-4
Sucrose	Merck	Cat#57-50-1
HEPES	Merck	Cat#7365-45-9
KCl	Merck	Cat#77447-40-7
$MgCl_2$	Merck	Cat#7786-30-3
DTT	Merck	Cat#3483-12-3
RNasin	Merck	Cat#R1158
RIPA buffer	Cell Signaling Technology	Cat#9806
Phenylmethylsulfonyl fluoride (PMSF)	Sigma	Cat#329-98-6
Protease plus phosphatase inhibitors	Thermo Scientific™	Cat#78440
Hoechst 33342	Invitrogen	Cat#R37165
Micrococcal Nuclease	Cell Signaling Technology	Cat#10011
Critical commercial assays		
PCR-based mycoplasma testing	Minerva Biolabs	Cat#11-8250
TRIzol	Sigma	Cat#T9424
High-quality reverse transcriptase and cDNA synthesis reagents	TaKaRa	Cat.#6210A
TB Green® Premix Ex Taq™ II	TaKaRa	Cat.#RR820B
Experimental models: Cell lines		
A375	ATCC	Cat.#CRL-1619
SK-MEL-28	ATCC	Cat.#HTB-72
QBC939	ATCC	Cat.#PDM-219

(*Continued on next page*)

Continued

REAGENT or RESOURCE	SOURCE	IDENTIFIER
WM983B	L. Larue (Institut Curie, France)	N/A
HEK293T	ATCC	Cat.#CRL-3519
YUMM1.7	ATCC	Cat #CRL-3362
YUMM2.1	MERCK	SCC232
Experimental models: Organisms/strains		
Female athymic nude Foxn1null mice	GemPharmatech Co., Ltd.	Strain NO. D000521
Oligonucleotides		
shcMyc1 Mature Antisense: TTCAAGTTTGTGTTTCAACTG	Horizon TRC library	TRCN0000039640
shcMyc2 Mature Antisense: TTGTTGCTGATCTGTCTCAGG	Horizon TRC library	TRCN0000039642
cMyc Forward: CCTGGTGCTCCATGAGGAGAC	This paper	N/A
cMyc Reverse: CAGACTCTGACCTTTTGCCAGG	This paper	N/A
pre-rRNA Forward: GCTCTACCTTACCTACCTGG	This paper	N/A
pre-rRNA Reverse: TGAGCCATTCGCAGTTTCAC	This paper	N/A
ATF4 Forward: ATGACCGAAATGAGCTTCCTG	This paper	N/A
ATF4 Reverse: GCTGGAGAACCCATGAGGT	This paper	N/A
E2F4 Forward: CACCACCAAGTTCGTGTCCC	This paper	N/A
E2F4 Reverse: GCGTACAGCTAGGGTGTCA	This paper	N/A
SDHB Forward: ACAGCTCCCCGTATCAAGAAA	This paper	N/A
SDHB Reverse: GCATGATCTTCGGAAGGTCAA	This paper	N/A
5s rRNA Forward: GGCCATACCACCCTGAACGC	This paper	N/A
5s rRNA Reverse: CAGCACCCGGTATTCCCAGG	This paper	N/A
RPS6 Forward: GCCACAGAAGTTGCTGCTGACG	This paper	N/A
RPS6 Reverse: GGTCAAGACACCCTGCTTCATG	This paper	N/A
RPS15 Forward: CAGCATGGTGGGCGTCTACAAC	This paper	N/A
RPS15 Reverse: GCTTGTAGGTGATGGAGAACTCG	This paper	N/A
RPL7 Forward: GAGGATGGCAAGAAAAGCTGGC	This paper	N/A
RPL7 Reverse: CGAACCTTTGGGCTCACTCCAT	This paper	N/A
RPL11 Forward: AGAGTGGAGACAGACTGACGCG	This paper	N/A
RPL11 Reverse: CGGATGCCAAAGGATCTGACAG	This paper	N/A
RPS26 Forward: TAACTGTGCCCGATGCGTG	This paper	N/A
RPS26 Reverse: GCTCGCTTCAGAAATGTCCC	This paper	N/A
HPRT1 Forward: CATTATGCTGAGGATTTGGAAAGG	This paper	N/A
HPRT1 Reverse: CTTGAGCACACAGAGGGCTACA	This paper	N/A
cMyc-CCND1 Forward: GCCGGAATGAAACTTGCACA	This paper	N/A
cMyc-CCND1 Reverse: CAGAATGGGCGCATTTCCAA	This paper	N/A
cMyc-RPS6 Forward: TCTTGACTGCTACTCTGCTTTCACG	This paper	N/A
cMyc-RPS6 Reverse: AGCCTTTCATGTTGCCTCCACAC	This paper	N/A
cMyc-RPL7L Forward: GAAGCCGCAGTATAGAGGGG	This paper	N/A
cMyc-RPL7L Reverse: TCTCTGGGGAGGAAGACAGG	This paper	N/A
cMyc-RPL39 1 Forward: GCAGCCAAGGAAGAGGTTCT	This paper	N/A
cMyc-RPL39 1 Reverse: AGTGCCATTTTCCCAGAGGG	This paper	N/A
Software and algorithms		
GraphPad Prism 8	GraphPad	RRID: SCR_002798
Xtail	R studio	https://github.com/xryanglab/xtail
Deposited data		
A375 polysome mass spectrometry	This paper	Deposited to ProteomeXchange Consortium: PXD052572

(*Continued on next page*)

Continued

REAGENT or RESOURCE	SOURCE	IDENTIFIER
Polysome RNA sequencing	This paper	Deposited to Gene Expression Omnibus: GSE313946
Murine melanoma RNAseq	Song et al.	GEO: GSE75313
Human melanoma RNAseq	Hugo et al.	GEO: GSE65186

EXPERIMENTAL MODEL AND STUDY PARTICIPANT DETAILS

Experimental animals

Female athymic nude *Foxn1null* mice aged 6-8 weeks were used for the *in vivo* xenograft experiments. Mice were housed in pathogen-free conditions with *ad libitum* food and water. Animal experiments were conducted following CCAC guidelines and protocols, and were approved by the ethical committee of West China Hospital of Sichuan University (Ethical Approval No. 20220107014). Female mice were specifically selected for these experiments because their relatively docile nature facilitates handling, thereby minimizing the risk of excessive stress or injury to the animals. The sex of the mice is not considered a biological variable that influences or is associated with the outcomes of this study.

Cell lines

The human cell lines A375, SK-MEL-28, and QBC939, as well as the mouse cell line YUMM1.7, were purchased from the American Type Culture Collection (ATCC). The YUMM2.1 cell line was obtained from Merck, and the melanoma cell line WM983B was kindly provided by L. Larue (Institut Curie, France). Commercial cell lines were authenticated by their respective vendors prior to purchase (e.g., ATCC provides a Certificate of Analysis including comprehensive STR profiling for human cell lines); therefore, no additional *de novo* STR authentication was performed in-house. All cell lines were maintained according to standard protocols and subjected to periodic PCR-based testing (Minerva Biolabs, China) to confirm their strict mycoplasma-free status.

Human subjects

This study utilized previously published transcriptomic datasets from biopsies of melanoma patients (GEO: GSE65186). No new human subjects were recruited or sampled for this study, and all human sample data were derived entirely from publicly available databases. Consequently, the reporting of institutional oversight, ancestry, race, or ethnicity is not applicable to this study.

Reagents

All the cell lines were incubated at 37 °C with 5% CO2 in a humidified environment. They were cultured in DMEM growth media supplemented with 10% FBS and 2 mM glutamine (Gibco), except for SK-MEL-28 cells, which were cultured in RPMI1640 supplemented with 10% FBS. All cell lines were subjected to periodic PCR-based testing (Minerva Biolabs) to confirm their mycoplasma-free status. BRAF inhibitor (Vemurafenib, #S1267), MEKi (Cobimetinib, #S8041), Homoharringtonine (CGX-635, #S9015), Harringtonine (#S9063), Gemcitabine (#S1714), Cisplatin (#S1166) were purchased from Selleck.cn (China). Cycloheximide (CHX, #C104450) was purchased from Sigma. PLX-4720 (BRAFi, #918505-84-7) and PD0325901(MEKi, #391210-10-9) were purchased from Lebomei (China). Dimethylsulfoxide (DMSO) was employed as the solvent to dissolve all chemicals for *in vitro* investigations.

Production of drug-tolerant persister cells

For the generation of persister cells, melanoma parental cells were treated with Vemurafenib (1μM) and Cobimetinib (500 nM) for 72 h. Cell line QBC9393 was used to produce cholangiocarcinoma persisters. Parental QBC9393 cell were treated with Gemcitabine (10μM) and Cisplatin (5μM). Approximately 80% of parental cells will be killed by combination treatment and detach from the culture dish. The surviving cells that remained attached were trypsinized and then rinsed once with phosphate-buffered saline (PBS). The retrieved persister cells were replaced in drug-free growth medium till next day to conduct experiments such as western blotting analysis, polysome profiling and quantitative RT-PCR. Parental cells treated with DMSO served as the control group in the experiments.

METHOD DETAILS

Polysome profiling measuring translational activity

Polysome profiling was conducted following previously described methods.[7] Firstly, cells subjected to specific treatments were incubated at 37 °C with 100 μg/mL cycloheximide in fresh medium for 5 minutes. Afterward, the cells were washed and scraped into ice-cold PBS containing 100 μg/mL cycloheximide, followed by centrifugation at 3000 rpm for 5 minutes. The resulting cell pellets were resuspended in 400 μL of LSB buffer (1.5 mM KCl, 2.5 mM MgCl2, 5 mM Tris, pH 7.5, 100 U/mL RNasin, 2 mM DTT, 1x protease and phosphatase cocktail inhibitors, and 100 μg/mL cycloheximide). After homogenization, 0.5% Triton X-100 and 0.5% sodium deoxycholate were added to the 400 μL of LSB buffer to reach a total volume of 500 μL. The samples were kept on ice for 30 minutes and

then centrifuged at 12,000 g and 4 °C for 15 minutes. The lysates were quantified using a NanoDrop spectrophotometer, and their concentrations were normalized by adding hypotonic buffer according to the OD260 value. To prepare the sucrose gradient, a 60% (w/v) sucrose solution in ddH2O was made and filtered through a 0.22 μm filter to prevent tubing clogging. A 10x sucrose gradient buffer was prepared by dissolving 200 mM HEPES (pH 7.6), 1 M KCl, 50 mM MgCl2, 100 μg/mL cycloheximide, 1x protease inhibitor cocktail (EDTA-free), and 100 U/mL RNase inhibitor in 5 mL ddH2O. By using the 60% sucrose solution, 5% and 50% sucrose solutions in 1x sucrose gradient buffer were prepared, and the density gradient was made using a Gradient master machine. The normalized lysates were then carefully loaded onto a sucrose density gradient ranging from 5% to 50%. Subsequently, the gradients were subjected to centrifugation at 36,000 rpm for 2 hours at 4 °C using an SW41 Ti rotor (Beckman). After centrifugation, polysome fractions were monitored and collected using a gradient fractionation system (Isco).

Clonogenic assay

In order to produce drug-resistant clones from individual cells, the cells were cultured for approximately 10 passages in drug-free growth medium. The cells were subsequently plated at low density (5000 cells per well in 6-well plates) in fresh medium. 24 hours later, the cells were exposed to either drugs or DMSO at the specified concentrations, with two replicate wells per condition. 2 weeks later, the cells were rinsed once with PBS and then fixed with 4% paraformaldehyde solution for 12 minutes at room temperature. Following fixation, the cells were dyed with a 0.5% (weight/volume ratio) crystal violet in 70% ethanol. In order to assess the clonogenic capacity of persister cells following various drug combination schedules, melanoma persister cells were produced by exposing them to Vemurafenib (1μM) and Cobimetinib (500 nM) simultaneously for 72 hours. The cells that persisted after the treatment were then seeded in 6-well plates at a low cell concentration. Cells were then treated with different combination treatment schedules for 6 weeks. As a control, cells were left in growth medium containing 10% FBS and DMSO. After 6 weeks, the cells were washed once with cold PBS and fixed using a 4% paraformaldehyde solution for 12 minutes at room temperature. After fixation, the cells were stained with 0.5% (weight/volume ratio) crystal violet in 70% ethanol solution. Image analysis was performed to assess Colony Area.

Western blotting analysis

Western blotting was conducted using cell extracts from parental and persister cells treated with the specified drug concentrations. Whole cell lysates were generated in RIPA buffer (Cell Signaling Technology) supplemented with phenylmethylsulfonyl fluoride (Sigma), dithiothreitol (DTT), and protease plus phosphatase inhibitors (Roche). Lysate protein content was measured by bicinchoninic acid assay (Invitrogen). Proteins were separated by gel electrophoresis using 4-12% Bis-Tris NuPAGE gels with MOPS or 3-8% Tris-acetate gels with Tris-acetate buffer (Life Technologies), then transferred to 0.45 um nitrocellulose (Amersham). Membranes were blocked with 5% milk in Tris-buffered saline before overnight 4°C incubation with agitation in primary antibodies diluted 1:1000. c-Myc (Cell Signaling Technology, rabbit, #9402s), RPL7 (Proteintech, rabbit, #14583-1-AP), RPS15 (Proteintech, rabbit, #14957-1-AP), RPS6(Cell Signaling Technology, rabbit, #2217). Horseradish peroxidase (HRP)-conjugated secondary antibodies were purchased from Sigma.

Lentiviral shRNA stable cell lines

Lentiviral shRNA constructs targeting specific genes were purchased from Horizon TRC library. Validated constructs were selected (Horizon). Lentivirus was produced by co-transfecting shRNA constructs with pMD2.G, pRRE and pRSV/REV packaging plasmids into HEK293T cells using Calfectin (ThermoFisher). Viral supernatants were collected 24h, 48h and 72h post-transfection, centrifuged at 3000 rpm 10 minutes and 0.45 μm filtered. Lentivirus was aliquoted and stored at -80°C. A375 cells were transduced to generate stable knockdowns (shc-Myc, shNTC) under 1 μg/mL puromycin selection.

shc-Myc1 (TRCN0000039640) Mature Antisense:
TTCAAGTTTGTGTTTCAACTG
shc-Myc2 (TRCN0000039642) Mature Antisense:
TTGTTGCTGATCTGTCTCAGG

RNA isolation and quantitative RT-PCR

RNA was extracted with TRIzol (Sigma) following manufacturer's instructions and quantified by NanoDrop 2000 (Thermo Scientific), then normalized to 20 ng/mL in RNase-free water. 200 ng RNA was reverse transcribed into cDNA using High-quality reverse transcriptase and cDNA synthesis reagents for PCR (TaKaRa). mRNA abundance was determined by qPCR using TB Green® Premix Ex Taq™ II (TaKaRa) and indicated primers. Data was analyzed by the comparative Ct method relative to HPRT. Primers used in this study were as follows:

c-Myc	Forward	CCTGGTGCTCCATGAGGAGAC
c-Myc	Reverse	CAGACTCTGACCTTTTGCCAGG

(*Continued on next page*)

Continued		
pre-rRNA	Forward	GCTCTACCTTACCTACCTGG
pre-rRNA	Reverse	TGAGCCATTCGCAGTTTCAC
ATF4	Forward	ATGACCGAAATGAGCTTCCTG
ATF4	Reverse	GCTGGAGAACCCATGAGGT
E2F4	Forward	CACCACCAAGTTCGTGTCCC
E2F4	Reverse	GCGTACAGCTAGGGTGTCA
SDHB	Forward	ACAGCTCCCCGTATCAAGAAA
SDHB	Reverse	GCATGATCTTCGGAAGGTCAA
5s rRNA	Forward	GGCCATACCACCCTGAACGC
5s rRNA	Reverse	CAGCACCCGGTATTCCCAGG
RPS6	Forward	GCCACAGAAGTTGCTGCTGACG
RPS6	Reverse	GGTCAAGACACCCTGCTTCATG
RPS15	Forward	CAGCATGGTGGGCGTCTACAAC
RPS15	Reverse	GCTTGTAGGTGATGGAGAACTCG
RPL7	Forward	GAGGATGGCAAGAAAAGCTGGC
RPL7	Reverse	CGAACCTTTGGGCTCACTCCAT
RPL11	Forward	AGAGTGGAGACAGACTGACGCG
RPL11	Reverse	CGGATGCCAAAGGATCTGACAG
RPS26	Forward	TAACTGTGCCCGATGCGTG
RPS26	Reverse	GCTCGCTTCAGAAATGTCCC
HPRT1	Forward	CATTATGCTGAGGATTTGGAAAGG
HPRT1	Reverse	CTTGAGCACACAGAGGGCTACA

Mouse xenograft experiments

Mice were housed in pathogen-free conditions with *ad libitum* food/water and animal experiments were conducted following CCAC guidelines and protocols approved by the ethical committee of West China Hospital of Sichuan University. Mice were allocated to groups with matched starting mean tumor volumes. The investigator was not blinded. Female athymic nude Foxn1null mice aged 6-8 weeks were injected subcutaneously in right flank with 5x106 A375 cells in 100μL PBS. At 400mm3 mean tumor volume, mice were fed control diet or diet with 200ppm PLX-4720 (BRAFi) and 7ppm PD0325901 (MEKi). Homoharringtonin (HHT, 0.5mg/kg) was injected intraperitoneally three times weekly. Tumor dimensions were measured every two days by digital caliper. Tumor volume was calculated by the formula L x W2 x 0.5 (L=length, W=width).

Immunofluorescence microscopy

The 4% paraformaldehyde (PFA) solution was used to fix cells for 15 minutes at room temperature, followed by permeabilization with 0.1% Triton X-100 for 10 minutes. Cells were blocked with 5% bovine serum in PBS to prevent non-specific binding, followed by staining overnight at 4°C using primary antibodies against Ki67, PES1, NPM1. Secondary antibodies conjugated to appropriate AlexaFluor fluorophores were used for detection. Nuclei were counterstained with 10mM Hoechst 33342 (Molecular Probes-Invitrogen). Imaging was performed by confocal microscopy using a LSM 150 microscope (Carl Zeiss, Jena, Germany).

Image-based supervised classification using CellProfiler

Fluorescence images were acquired using identical exposure settings across all experimental conditions and saved as 16-bit TIFF files without prior processing. Image analysis was performed using CellProfiler (v4.0) and CellProfiler Analyst (v3.0). Nuclear segmentation was conducted on the DAPI channel using the IdentifyPrimaryObjects module with a typical object diameter of 20-60 pixels. Global thresholding was applied using the Otsu three-class method with a threshold correction factor of 1.0 and a smoothing scale of 1.0. Clumped nuclei were separated using shape-based de-clumping with intensity-based watershed and a local maxima suppression distance of 5 pixels. Objects touching image borders were excluded from analysis. Following segmentation, single-cell features were extracted from both DAPI and NPM1 channels using MeasureObjectIntensity, MeasureTexture, MeasureGranularity, and MeasureObjectSizeShape modules. Extracted features included mean, median, and integrated intensity, intensity standard deviation, area, perimeter, eccentricity, solidity, Haralick texture features (scales 3 and 5), and granularity spectrum features (1-10). No manual threshold adjustment was performed beyond the predefined segmentation parameters. Single-cell measurements were exported to CellProfiler Analyst for supervised machine learning classification. Cells were manually annotated into positive and negative phenotypic categories to generate a training set comprising approximately 50-100 cells per class across multiple images.

Classification was performed using a Random Forest classifier with 100 trees and default depth settings, incorporating all extracted morphological, intensity, texture, and granularity features with Z-score normalization. Classifier performance was iteratively refined through inspection of misclassified cells until stable discrimination was achieved. The trained classifier was subsequently applied to independent experimental datasets for automated single-cell phenotype assignment. For each condition, four randomly selected regions of interest were analyzed, with a total of 100 nuclei quantified per condition.

TMT based quantitative mass spectrometry

After conducting polysome profiling, the sucrose-based fractions containing monosomes and polysomes from parental and DTP cells were pooled separately. Each combined fraction was mixed with four times the volume of methanol, three times the volume of ultra-pure water, and the same volume of chloroform. The mixture was then centrifuged at 17,000g for 5 minutes. After centrifugation, the top water layer was carefully removed, and an equal volume of methanol was added to the remaining solution. The protein was subsequently precipitated by centrifugation at 17,000g for 15 minutes. The resulting protein pellets were resuspended in DB dissolution buffer (8 M Urea, 100 mM TEAB, pH 8.5) and subjected to 5 minutes of ultrasonication on ice. The lysate was then treated with 1M DTT at 56°C for 1 hour, followed by alkylation with iodoacetamide in the dark at room temperature for 1 hour, and a subsequent 2-minute ice bath. The protein concentration of each sample was determined using the BCA assay, following the instructions of the Bradford protein quantity kit (Thermo Fisher Scientific).

The volume of each protein sample was adjusted to 100 μL with DB dissolution buffer. The samples were mixed and digested with trypsin and 100 mM TEAB buffer at 37°C for 4 hours, and then trypsin and CaCl2 were added for overnight digestion. The digested samples were adjusted to pH below 3 by mixing with formic acid and centrifuged at 12,000g for 5 minutes at room temperature. The resulting supernatant was carefully applied to a C18 desalting column, and the column was washed three times with a washing buffer containing 0.1% formic acid and 3% acetonitrile. Subsequently, the elution buffer consisting of 0.1% formic acid and 70% acetonitrile was used to elute the samples from the column. The eluents from each sample were collected, and the solvent was removed through a process of lyophilization.

To label the samples with TMT, each sample containing 50 μg of protein was mixed with 100 μL of 0.1 M TEAB buffer. Then, 41 μL of TMT labelling reagent dissolved in acetonitrile was added to the mixture. The sample was thoroughly shaken for 2 hours at room temperature to ensure proper mixing. The labeling reaction was terminated by adding 8% ammonia. All labeled samples were combined in equal volumes, subjected to desalting, and then lyophilized. For subsequent analysis, a gradient elution method was employed using mobile phase A (2% acetonitrile, pH adjusted to 10.0 with ammonium hydroxide) and mobile phase B (98% acetonitrile). The lyophilized powder was reconstituted in solution A, followed by centrifugation at 14,000g for 20 minutes at 4°C. The reconstituted samples were fractionated using a C18 column (Waters BEH C18, 4.6×250 mm, 5 μm) on a Rigol L3000 HPLC system, with the column temperature set to 45°C. The eluates were monitored at a wavelength of 214 nm using UV detection, and one tube was collected per minute. These collected fractions were then combined to form a total of 10 fractions. Subsequently, all fractions were dried under vacuum, reconstituted in a solution consisting of 0.1% (v/v) formic acid (FA) in water, and prepared for UHPLC-MS/MS analysis.

The UHPLC-MS/MS analysis was conducted using a Thermo Fisher EASY-nLC 1200 UHPLC system, coupled with a Thermo Fisher Q Exactive HF-X mass spectrometer. The separated peptides were subjected to analysis by the Q Exactive HF-X mass spectrometer using the Nanospray Flex (ESI) ion source. The ion source was operated with a spray voltage of 2.3 kV, and the ion transport capillary temperature was maintained at 320°C.During the analysis, full scans were performed in the mass-to-charge ratio (m/z) range of 350 to 1500, with a resolution of 60,000 (at m/z 200). The automatic gain control (AGC) target value was set to 3×106, and the maximum ion injection time was limited to 20 ms. The top 40 precursor ions with the highest abundance in the full scan were selected for fragmentation using higher energy collisional dissociation (HCD) and analyzed in MS/MS mode. The resolution for MS/MS was set at 45,000 (at m/z 200) for 10 plex. Additional parameters included an AGC target value of 5×104, a maximum ion injection time of 86 ms, a normalized collision energy of 32% for fragmentation, an intensity threshold of 1.2×105, and a dynamic exclusion parameter set to 20 seconds. These settings ensured efficient and accurate data acquisition during the UHPLC-MS/MS analysis. Extracted tryptic peptides underwent data-independent acquisition (DIA) analysis using a nanoAcquity UPLC system connected to a Waters Synapt G2-S HDMS mass spectrometer. Proteins were quantified by the ISOQUANT "TOP 3" method.

Harringtonine run-off assays

Harringtonine stalls 80S ribosomes at start codons, blocking further elongation.[30] Polysome run-off the mRNA and the loss rate of ribosomes was measured by sucrose density gradients centrifugation.[72] Translation was blocked with 2mg/ml harringtonine for 180 seconds, followed by 100μg/ml cycloheximide for 3 minutes. Cells were lysed in buffer (20mM Hepes pH7.5, 150mM NaCl, 3mM MgCl2, 0.2M sucrose, 0.5% NP40, cycloheximide, protease inhibitors, RNase inhibitor). Equal total protein from the different extracts was resolved by 10-50% sucrose gradient fractionation.

Chromatin immunoprecipitation (ChIP)-quantitative PCR

According to the manufacturer's experimental procedure, 4x106 cells were used for each ChIP assay. After using 37% formaldehyde to crosslink cell proteins and DNA, cells were resuspended in douncing buffer (10mM Tris-HCl pH7.5, 4mM MgCl2, 1mM CaCl2, protease inhibitors), dounced and homogenized. Chromatin was digested with Micrococcal Nuclease (Cell Signaling Technology, #10011) at 37°C for 20 minutes, stopped with 0.5M EDTA. Chromatin was resuspended in hypotonic buffer (0.2mM EDTA pH8.0,

0.1mM benzamidine, 0.1mM PMSF, 1.5mM DTT, protease inhibitors) and incubated 1 hour on ice. Cell debris was pelleted and supernatant recovered. Chromatin was precleared with protein A/G dynabeads (Life Tech) then immunoprecipitated overnight at 4°C with c-Myc antibody (Cell Signaling Technology, #9402). Complexes were washed with ChIP wash buffers I and II. Complexes were eluted 2 hours at 68°C in elution buffer (100mM NaHCO3, 1% SDS). Immunoprecipitated material was phenol-chloroform purified and 5ng used for library construction. Subsequent quantitative RT-PCR primers used in this study were as follows:

CCND1	Forward	GCCGGAATGAAACTTGCACA
CCND1	Reverse	CAGAATGGGCGCATTTCCAA
RPS6	Forward	TCTTGACTGCTACTCTGCTTTCACG
RPS6	Reverse	AGCCTTTCATGTTGCCTCCACAC
RPL7L	Forward	GAAGCCGCAGTATAGAGGGG
RPL7L	Reverse	TCTCTGGGGAGGAAGACAGG
RPL39	Forward	GCAGCCAAGGAAGAGGTTCT
RPL39	Reverse	AGTGCCATTTTCCCAGAGGG

Polysome RNA extraction

Lysates of Yumm1.7 and A375 parental and DTP cells were separated into polysome fractions after sucrose gradient centrifugation (as described above). Polysome RNA extraction was performed using 1.5 mL Eppendorf tubes on ice, with prepared reagents including TRIzol-LS for RNA extraction from liquid, chloroform, isopropanol, and 75% ethanol. For the last four fractions, 300μl from each of three fractions plus 100μl from the final fraction were merged to a total of 1 ml sucrose solution, mixed well, and aliquoted into five tubes at 200μl per tube. To each tube, including the input with a volume less than 200μl, 800μl TRIzol-LS was added, followed by the addition of 400μl chloroform at a fraction-to-chloroform ratio of 1:2. The tubes were shaken violently by hand for at least 15 seconds and allowed to sit for stratification for around 2 minutes, then centrifuged at 12,000 g for 15 minutes at 4°C. After centrifugation, three layers were observed: the aqueous water layer, protein layer, and organic layer, and the top water layer was carefully collected while avoiding the thin white protein layer. An additional 400μl chloroform was added, and the shaking, sitting, centrifugation, and aqueous layer collection steps were repeated. To the collected aqueous phase, 1 mL isopropanol and 2.5 μl Glycoblue were added, followed by vortexing for at least 10 seconds and incubation at -20°C overnight. Samples were then centrifuged at 12,000 g for 30 minutes at 4°C, the supernatant was removed carefully without disturbing the pellet, and pellets from all five tubes were collected in 1 mL 75% ethanol, vortexed, and centrifuged at 17,000 g for 15 minutes at 4°C. The supernatant was removed, the pellets were air-dried, and 20-50μl DEPC-treated or ultrapure water was added followed by vortexing. Finally, RNA concentration was determined using a NanoDrop spectrophotometer, quality was assessed by loading on an agarose gel, and samples were stored at -80°C.

Polysome RNA library preparation for transcriptome sequencing

Polysome RNA served as the input material for RNA sample preparations. Briefly, mRNA was purified from polysome RNA using poly-T oligo-attached magnetic beads. Fragmentation was performed with divalent cations at elevated temperature in 5X First Strand Synthesis Reaction Buffer. First-strand cDNA was synthesized using random hexamer primers and M-MuLV Reverse Transcriptase, followed by RNA degradation with RNase H. Second-strand cDNA synthesis was then carried out using DNA Polymerase I and dNTPs. Remaining overhangs were converted to blunt ends through exonuclease/polymerase activities. Following adenylation of the 3' ends of DNA fragments, adaptors with hairpin loop structures were ligated to prepare for hybridization. To select cDNA fragments preferentially 370–420 bp in length, library fragments were purified using the AMPure XP system (Beckman Coulter, Beverly, USA). PCR amplification was subsequently performed, and the PCR products were purified with AMPure XP beads to obtain the final library.

To ensure library quality, testing was conducted post-construction. The library was initially quantified using a Qubit 2.0 Fluorometer, diluted to 1.5 ng/μL, and insert size was assessed with an Agilent 2100 Bioanalyzer. Once the insert size met expectations, qRT-PCR was employed to precisely quantify the effective library concentration (requiring >1.5 nM) for quality assurance. Qualified libraries were pooled based on effective concentration and target data output, then sequenced on the Illumina NovaSeq 6000 platform, generating 150 bp paired-end reads. Sequencing operated on the principle of synthesis by sequencing (Sequencing by Synthesis), where four fluorescently labeled dNTPs, DNA polymerase, and splice primers were added to the flow cell for amplification. As sequence clusters extended complementary strands, each fluorescently labeled dNTP released corresponding fluorescence. The sequencer captured these signals, converting optical data into sequencing peaks via computer software to derive the sequence information of tested fragments.

Polysome RNA bioinformatics analysis - Xtail

Image data from the high-throughput sequencer were converted into sequence data (reads) via CASAVA base calling. Raw data (raw reads) in FASTQ format were first processed using in-house Perl scripts. During this step, clean data (clean reads) were generated by removing adapter-containing reads, reads with N bases, and low-quality reads from the raw data. Simultaneously, Q20, Q30, and GC content of the clean data were calculated. All subsequent analyses were performed using the high-quality clean data. Reference genome and gene model annotation files were downloaded directly from the genome website. An index of the reference genome was constructed using Hisat2 (v2.0.5), and paired-end clean reads were aligned to the reference genome with the same tool. Hisat2 was chosen as the mapping software because it generates a database of splice junctions from the gene model annotation file, yielding superior alignment results compared to other non-splice-aware mapping tools.

Differential translation analysis was conducted using the Xtail R package, a specialized tool designed for ribosome profiling data to identify genes exhibiting differential translation between experimental conditions by simultaneously evaluating changes in mRNA abundance and ribosome-protected fragments (RPFs). Xtail assesses translational efficiency by comparing log2 fold changes (log2FC) between RPF and mRNA levels across conditions, as well as log2 ratios (log2R) of RPF to mRNA within each condition, modeling read counts with negative binomial distributions via DESeq2 for parameter estimation and normalization. It generates posterior distributions to infer the magnitude and significance of differential translation, selecting the more conservative P-value from parallel pipelines, with adjustments for multiple testing using the Benjamini-Hochberg method to control the false discovery rate. Genes were considered significantly differentially translated if the adjusted P-value (padj) was $\leq$ 0.05 and the absolute log2 fold change was $\geq$ 1.

QUANTIFICATION AND STATISTICAL ANALYSIS

All experiments were performed in three independent biological replicates. Experimental data were analyzed using GraphPad Prism 8 (GraphPad, USA). Statistical analysis was done using GraphPad Prism 8 (GraphPad, USA). Data are presented as mean ± SEM or mean ± SD. Two-group comparisons were made by unpaired two-tailed Student's t-test. One-way ANOVA was used for multi-group comparisons. P values <0.05 were considered significant (*p<0.05; **p<0.01; ***p<0.001; ****p<0.0001).